Isotope effect in plasmas driven by ECR modules towards H− and D− production

M Mitrou, P Svarnas, S Béchu, S Aleiferis

Plasma Sources Science and Technology

Isotope effect in plasmas driven by ECR modules towards H^- and D^- production

To cite this article before publication: Maria Mitrou *et al* 2023 *Plasma Sources Sci. Technol.* in press https://doi.org/10.1088/1361-6595/acfbf5

Isotope effect in plasmas driven by ECR modules towards H^- and D^- production

M. Mitrou[1,2], P. Svarnas[1, a)], S. Béchu[2], S. Aleiferis[3]

[1]High Voltage Laboratory, Electrical and Computer Engineering Department, University of Patras, Rion-Patras 26504, Greece

[2]Université Grenoble Alpes, CNRS, Grenoble INP (Institute of Engineering), LPSC-IN2P3, 38000 Grenoble, France

[3]EUROfusion consortium, JET, CCFE, Culham, Science Centre, Abingdon Ox14 3DB, United Kingdom

[a)] Author to whom correspondence should be addressed: svarnas@ece.upatras.gr

Abstract

Optimization of negative ion sources operated with deuterium may be limited by the lack of data on fundamental processes. Insight can be obtained from studies focusing on a direct comparison of H_2 and D_2 plasmas. Herein, the ECR volume negative ion source "Prometheus I" operates with both H_2 and D_2 gases and the properties of the generated plasmas are probed by means of electrostatic probe and laser induced photo-detachment. A parametric study, involving pressure and microwave (2.45 GHz) power variation, reveals similar qualitative trends for most of the plasma properties in both gases. However, quantitively, differences do exist for the plasma potential, the electron density and temperature, and the negative ion to electron density ratio. EEDFs are thus isotope dependent. Overall, nearly the same maximal H^- and D^- negative ion densities are achieved (i.e., 4×10^9 cm^{-3}). The results are eventually elucidated with respect to the ECR heating mechanism, and the production and destruction paths of the negative ions.

Keywords. ECR plasmas; Negative ions; Hydrogen; Deuterium; Photo-detachment; Probes.

I. Introduction

The heating and current drive of the plasma in ITER will rely on the injection of a total of 33 MW of 1 MeV D^0 [1,2]. The formation of these powerful D^0 beams will be based on the neutralization of accelerated D^- beams since, at such high energies, the efficiency of this process remains acceptable (~56%) for negative ions but becomes unsuitably low for positive ions [2,3]. ITER's neutral beam cell will be equipped with four injectors: three heating neutral beams (the third will be employed in the event of a future upgrade to 50 MW of injected power), and a diagnostic neutral beam [4]. The most critical component of a heating neutral beam is the negative ion source itself, expected to provide either a 1 MeV D^- beam or a 0.87 MeV H^- beam of an accelerated current density of 200 A m^{-2} or 260 A m^{-2} and an accelerated current of 40 A or 46 A, for a duration of 3600 s or 1000 s, respectively, operating in both cases at a filling pressure of 0.3 Pa or less [1,2,4]. Operation with hydrogen is foreseen for the early, non-nuclear phases of ITER [2].

The only types of negative ion sources that have been deemed capable of meeting these requirements are the ones driven by Cs/arc or radio frequencies (RFs) [1]. However, an RF source was finally chosen to be utilized in ITER's injectors since it is free of filaments and thus there is no need for regular maintenance. This is in line with the concept for full remote handling during ITER's active phase [1,4]. ITER's source design follows a modular concept based on eight RF drivers, with each driver being based on the RF prototype source "BATMAN" [5-8]. In this type of source, negative ions are formed mainly through the surface production process [8,9].

The half-ITER-size ion source "ELISE" is an intermediate step towards the ITER neutral beam injector source that has been dedicated to resolve issues of technical or physical nature that inhibit the fulfillment of the ITER requirements [10,11]. Knowledge gained from "ELISE" is exploited by "SPIDER", a full-scale injector source. Though only able to provide a 100 keV neutral beam, research focuses on further optimization of the source performance, e.g., in terms of source uniformity over a beam area of about 1.5 m^2, negative ion current density, beam optics, beam source operation for 3600 s, and Cs distribution [12]. Eventually the second test bed, "MITICA", a complete full-scale injector embodying all ITER specifications, is foreseen to exhibit the overall target performance [12].

Up to date, "ELISE" has successfully demonstrated H^- pulses of 1000 s with a current density corresponding to 90% of the ITER goal [12]. On the other hand, the transition to deuterium has proven to be far more challenging as various complications stem from the inherent isotopic differences between hydrogen and deuterium. Some important issues are the generally higher, inhomogeneous, and less stable co-extracted electron current, the significantly larger amount of Cs needed for stabilizing this current, and the Cs depletion from the source walls and the plasma grid due to the higher atomic mass of deuterium [10,11]. Although considerable progress has been made after the application of refined Cs evaporation and distribution procedures, and though ITER requirements have nearly been reached for short D^- pulses, still only 66% of the ITER demand for negative ion current density can be extracted, over a time span of 45 min [10,11].

In line with the above brief presentation, it becomes apparent that any lab-scale fundamental study on a direct comparison between H_2 and D_2 plasma properties would be of added value. Indeed, this task has triggered the interest of different research groups, regardless of the type of the source employed. Namely:

As regards filament-driven sources, Cs-free discharges of both gases have been examined in the sources "Camembert II" and "Camembert III" [13,14]. The results indicate, briefly: (i) the electron density is consistently higher in D_2 with respect to H_2, in both sources; (ii) the electron temperature shows no significant change between H_2 and D_2 discharges in the larger source, as opposed to the smaller source in which it is lower in the case of H_2; (iii) the negative ion density and negative ion to electron density ratio is generally lower in D_2 than in H_2 in both sources, nevertheless these two parameters attain greater absolute values in the smaller source [14]. Observations (i) and (ii) have also been reported in the "Culham" source [15,16]. Additionally, in this latter source, a higher plasma potential has been measured in D_2 while the fast electron density and temperature remain the same in both H_2 and D_2. In another work in "Camembert II", two-laser photo-detachment has been used to infer the H^- and D^- ion temperatures, with the latter being lower [17]. Pure volume production of H^-/D^- in a rectangular arc chamber, with an external pair of permanent magnets in front of the plasma grid serving as a magnetic filter, has been the subject of other works [18,19]. Spatially resolved measurements with simultaneous variation of the magnetic filter field intensity revealed that the values for electron density and temperature were slightly higher in D_2 than in H_2. Furthermore, a stronger magnetic filter field is required to control the electron temperature in the D_2 plasma. In other filament-driven sources the isotope scaling has been investigated based on measurements of the extracted beam properties [20,21], along with probing of the characteristics of the plasma created in the vicinity of the extraction region [22,23]; the bottom line in the findings is that the extracted D^- ion current is constantly lower, accompanied by a larger co-extracted electron current. Moreover, the enhancing effects of Cs seeding on both H_2 and D_2 plasma properties, as opposed to Cs-free discharges, has been highlighted in studies at the "Camembert III" [24], "MANTIS" [25], and elsewhere [26]. In the filament driven "LIISA" ion source used at the "JYFL K130" cyclotron, the VUV emission spectra for both H_2 and D_2 have been compared. Neither the spectra nor the volumetric rates of ionization, excitation, production of high vibrational states, and dissociation between the two isotopes showed any significant difference. It is therefore suggested that in this source, the observed difference between the H^- and D^- production through dissociative electron attachment (DEA) is attributed most likely to the difference in the diffusion properties of hydrogen and deuterium [27].

As for inductively coupled plasma setups other than the prototypes described at the beginning of the present section, work [28] deals with the cases of H_2 and D_2 and shows that the atomic density is higher in D_2. Furthermore, atoms were found to be more efficiently ionized than the respective molecules, leading thus to a significantly elevated electron density in D_2 compared to H_2 and, consecutively, to a higher RF power transfer efficiency. Another setup, named "ACCesS", has been employed in experiments relevant to surface production of negative ions [29]. It was concluded that, no significant isotope effect occurs regarding the surface negative ion

formation. The reader is also referred to reports [30,31] for further studies concerning a comparison between surface production of H^- and D^-.

H_2 and D_2 discharges in RF-driven sources of a different type, i.e., helicons, have been studied in reference [32] as well as at the "RAID" source [33,34]. In [32] the density ratio of atomic to molecular deuterium was found to be higher than the respective ratio for hydrogen. In [33] the degree of dissociation and the ion densities were higher for deuterium than for hydrogen. In [34], the electron density was higher in the case of D_2, the electron temperature appeared to be nearly the same for H_2 and D_2, and the negative ion density and the negative ion to electron density ratio was lower in D_2.

Additionally, an electron cyclotron resonance (ECR) source with driven plasma rings has been studied in terms of extracted H^- and D^- ion current as a function of the pressure, the power, and the immersion depth of the plasma electrode into the plasma volume [35]. The D^- current was found to be less. Dissociative attachment of electrons to molecules at high Rydberg excited states was identified as the most probable process for H^- and D^- formation. Another ECR source, but of a tandem configuration, named "HOMER", has been studied for the case of H_2 [37,38]. In this source, the efficiency of materials with a low work function on the surface production of negative ions has also been investigated [39,40]. Particularly for the material MoLa, D_2 was also tested and while varying the isotope had an influence on the plasma parameters, the resulting effects on the negative ion formation compensated each other leading to comparable negative ion densities [39].

On the other hand, there is an alternative concept for ECR heating of H_2 and D_2 plasmas, based on the use of elementary dipolar ECR modules [41]. Negative ion sources reporting the use of this kind of ECR modules are "Camembert III" [42-46], "ROSAE III" [46,48], "SCHEME" [49,50], and "Prometheus I" [47,51-53]. "Camembert III" and "ROSAE III" have been operated and characterized in hydrogen only. "SCHEME", however, has been employed in experimental campaigns (i.e., synchrotron-based VUV absorption spectroscopy) involving both H_2 [49] and D_2 [50]. In summary, **Table I** provides the available data for the ECR sources of different configurations, including the data quoted by the present study.

Hereby, in the ECR volume source "Prometheus I", the research of the hydrogen plasma [47,50-53] is extended to deuterium. Basic plasma properties are accessed via probe measurements and laser-induced photo-detachment. The experiments are realized throughout the available range of the injected microwave (MW) power and the working pressure. The results are then compared and evaluated to identify similarities and differences between the ECR plasmas of the two isotopes. The isotope effect is mirrored on the electron energy distribution functions (EEDFs) of the H_2 and D_2 plasmas, and it is also noticeable on the negative ion to electron density ratio. Despite that, comparable H^- and D^- negative ion densities are achieved, and this apparent discrepancy is evaluated on a theoretical base.

II. Experimental setup

A conceptual design of the experimental setup is illustrated in **Fig. 1.** A thorough description of the negative ion source Prometheus I is given in [51-53]. Briefly, it consists of a 240 × 240 × 240 mm^3 (inner dimensions) stainless steel chamber with viewports for the installation of plasma diagnostics. The source is evacuated to a base pressure of around 5.33×10^{-5} Pa by a turbomolecular pump (Adixen ATP 80) backed up by a rotary pump (Adixen PASCAL 2021 SD). Operation within the pressure range of 0.13 – 2.67 Pa (measured by a MKS Baratron® 627D capacitance manometer) may be achieved by the insertion of either H_2 (99.999%; AirLiquide) or D_2 (99.8%; Linde) gas by means of a digital mass flow controller (MKS 1179B). Three representative pressures are here studied (0.53, 1.07 and 1.60 Pa; fixed when plasma ON). The plasma is sustained by an array of five elementary ECR modules [41] driven by independent solid-state microwave generators (SAIREM; 2.45 GHz), each capable of delivering a maximum power of 180 W. Herein, the injected power is varied from 30 to 180 W per module (0.15 to 0.9 kW in total).

Source wall conditioning requires special attention since, a notable difference in the plasma properties is observed when the two gases are interchanged. This effect can most likely be attributed to the adsorption of remainders of the formerly used gas into the interior surfaces of the source, also known as gas retention [54]. To ensure wall recovery, i.e., eliminate this issue and achieve stable and reproducible plasma properties, various trials led to the following protocol: each gas switch is followed by a bake-out of the source at 150°C, under base pressure conditions, for at least 30 h.

Throughout the experimental series, the temperature of the source walls is not controlled in any manner, therefore it is solely influenced by the operational parameters and the measurement sequence. However, it is monitored using a thermocouple for consistency reasons. In between measurements, a 20-min interval is allowed for the thermal stabilization of the source. **Table II** provides collective information on the experimental conditions for each value of the working pressure and for the minimum and maximum power settings.

The produced plasma is characterized by means of Langmuir probe and laser photo-detachment (**Fig. 1**). The probed area corresponds to the center of the source and at a 65 mm distance downstream of the midplane of the magnet of the central ECR module. The probe is made of a 0.25 mm in diameter tungsten wire and the tip (exposed to the plasma) is L-bent such that to be coaxially aligned with the laser beam for the photo-detachment measurements. The tip length is 15 mm in total with the bent part being 11 mm. The rest of the wire is housed in a telescopic configuration of dielectrics (an alumina tube inside a wider quartz tube) to insulate and protect it from the plasma. Part of the quartz tube is supported inside a stainless-steel tube that ends in a standard BNC vacuum feedthrough. A CF flange-to-quick connect coupling adapter makes a vacuum sealing with the steel tube and at the same time allows the linear translation of the probe [53]. I–V characteristic curves are acquired by a lab-made, automated system of high accuracy [55]. The probe voltage is swept from -70 V to 30 V with a step of 97.6563 mV. At each voltage step 2^{12} samples are averaged with a routine embedded in the system microcontroller, to increase

the signal-to-noise ratio. Prior to each acquisition, the tip surface is cleaned by heating induced by a high electron current, over 10 s which is then followed by another 10 s of cooling.

The processing of the I–V curves in order to gain access to main plasma parameters (i.e., plasma potential V_p, floating potential V_f, cold electron density $n_{e(cold)}$, and hot electron density $n_{e(hot)}$) has been described previously [53]. Briefly, the floating potential is defined as the potential for which the current collected by the probe equals zero, while the plasma potential is determined from the maximum of the first derivative of the I–V curve. The positive ion current is extrapolated linearly from the data at high retarding potentials and subsequently subtracted from the I–V curve. The remaining current, i.e., the electron current, is fitted as the sum of two exponentials, following iterative methods; residuals lower than 10% are achieved (**Figs. A1** and **A2**; Appendix). This points to a bi-Maxwellian electron energy distribution function (EEDF), implying two electron populations (hereafter "cold" and "hot" electrons). The density and temperature (quoted in eV) of the two populations, i.e., $n_{e(cold)}$, $n_{e(hot)}$ and $kT_{e(cold)}$, $kT_{e(hot)}$, respectively, are extracted from the fitting parameters of each exponential. Apart from the two exponentials, EEDFs are also constructed by using the Druyvesteyn method.

The components for the laser induced photo-detachment assembly are presented in **Fig. 1**. The laser employed (Nd:YAG; Quantel Brilliant EaZy) has the following specifications: 1064 nm (1.2 eV) photon wavelength (energy), 3 mm output beam radius, 330 mJ max energy per pulse, 10 ns pulse width, and 10 Hz repetition rate. The beam energy is precisely adjusted either by varying the delay between the laser flash lamp and the Q-switch or by the in-line installation of a half wave plate mounted on a precision rotational stage followed by a thin film polarizing beam splitter. This concept is based on Malus law and allows for the attenuation of the linearly polarized laser beam as a function of the angle between the beam's initial direction of polarization and the axis of the polarizer. **Fig. A3(a)** shows the corresponding calculated and measured attenuation curves.

Special attention is paid for the proper application of the photo-detachment technique [56]. Accordingly: (i) the beam radius set here, i.e., 2.5 mm, is larger than the probe collection radius (typical 0.1 mm under the present conditions). (ii) The beam energy density, i.e., 70 mJ cm^{-2} inside the vacuum chamber after considering an ~7% attenuation due to the glass viewport (**Fig. A3(a)**), suffices to detach the excess electron from all the negative ions within the irradiated volume. (iii) The probe bias voltage, i.e., +15 V, is adequate to collect all the photo-detached electrons around it. The impulse of the photo-detached electrons is recorded with a wideband current transformer (Pearson Electronics Inc.; Model 6585; 400 Hz - 250 MHz) on a digital oscilloscope (LeCroyWaveSurfer 104Xs-A; 1 GHz; 5 GSamples s^{-1}), without the use of a conventional decoupling circuit [57].

Regarding the laser beam energy density and the probe bias voltage, the above-mentioned values are justified by tests as those shown in **Figs. A3(b)** and **A3(c)**. In **Fig. A3(b)**, the theoretical relation [56] of the fraction of the detached ions as a function of the beam energy density is reproduced experimentally at typical operating conditions. The saturation of this fraction is predicted and also measured at energy densities as low as ~25 mJ cm^{-2}. In **Fig. A3(c)** the ratio between the peak of the photo-detached electron transient impulse and the steady state electron current versus an increasing probe bias voltage is presented. A positive probe bias of 15 V leads to

a quasi-saturation of this ratio. The plasma potential in D_2 is permanently higher than in H_2 (**Fig. A4**; Appendix) and the bias of 15 V is 1.5-3 times higher than any plasma potential measured, independently of the gas, pressure, and power. This value is also selected as a compromise between acceptable saturated ratio and prevention of the probe tip incandescence which takes place at higher bias voltages.

III. Results

In this section the main experimental results are categorized, compared, and primarily commented. A detailed discussion and physical interpretation of those is carried out in the next section; IV. Discussion. For now, as it has already been mentioned, we underline the production of two electron populations of different energies ("cold" and "hot") due to the heating induced by the present ECR design [58].

Fig. 2 gives the evolution of the cold electron density versus the MW power in both H_2 and D_2 plasmas, with the working pressure as a parameter. The order of magnitude of the density is between 10^{10} and 10^{11} cm^{-3}, while D_2 plasma is associated with higher cold electron densities independently of the pressure and the power level. In general, higher power or pressure leads to increased cold electron densities.

Fig. 3 presents the corresponding to **Fig. 2** results for the density of the hot electrons. It is reminded that the present study deals with the negative ion production region, i.e., the region downstream of the ECR driving region, and thus the hot electron population is not probed in its totality (see further discussion in Section IV). The absolute density was found to be about 2 orders of magnitude lower than that of the cold electrons. Furthermore, higher power or pressure leads to increased hot electron densities, similar to the cold electron case. On the other hand, the isotope effect seems to be less pronounced in the case of the hot population, since its density in the H_2 and D_2 plasmas tends to deviate less (compare **Figs. 2** and **3**).

The representative results of **Figs. A1** and **A2** in the Appendix, as well as previous studies [53], have shown that, the above-mentioned populations follow quasi-Maxwellian distributions. This fact has been confirmed over all the operational windows studied herein. **Figs. 4** and **5** provide a direct comparison of the EEDFs established in the H_2 and D_2 plasmas. To the best of our knowledge, a main gap exists in the literature as regards the study of the isotope effect on the EEDFs. Thus, the present results suggest divergence between the H_2 and D_2 plasma EEDFs. As it is expected, EEDFs are also pressure and power dependent (only the pressure dependence is given in **Figs. 4** and **5**). Such differences could regulate production and destruction processes of the H^- and D^- negative ions (see section IV).

The existence of an isotope effect for the EEDFs, as it is demonstrated in **Figs. 4** and **5**, is further supported if one considers the pressure and power dependence of the cold and hot electron energies in H_2 and D_2, and correlate them with the corresponding densities (**Figs. 2** and **3**). **Fig. 6** displays the existence of higher cold electron energies in the D_2 plasmas. Otherwise, the ECR heating leads to higher electron energies versus the MW power in both gases. The temperature of the hot electrons, downstream of the ECR zones, is almost constant (around 15 eV) at any experimental condition (**Fig. 7**) (see further discussion in Section IV).

Summarizing, D_2 plasma gives cold electrons of higher density and temperature than H_2 does under identical working conditions. H_2 and D_2 plasmas give, downstream of the ECR zones, hot electrons of comparable temperature whereas their density is either equal (**Fig. 3(b)**) or slightly higher (**Figs. 3(a)** and **3(c)**) in D_2, under identical working conditions. These features are reflected on the EEDF curves (**Figs. 4** and **5**). EEDFs with respect to the negative ion production/destruction are commented later.

Fig. 8 unveils the H^- and D^- negative ion density as either the MW power or the gas pressure increases. Higher values of both working parameters lead to higher densities of negative ions. It is worth noticing that the densities achieved are either equal (**Fig. 8(b)**) or slightly higher (**Figs. 8(a)** and **8(c)**) in H_2. In any case, values up to about 0.4×10^{10} cm^{-3} are reached in both the H_2 and D_2 plasmas.

Despite the close negative ion densities obtained in H_2 and D_2, the ratio of the negative ion to cold electron density is higher in the H_2 plasmas for any pressure and power level (**Fig. 9**). This ratio is an important parameter affiliated with the ratio of the negative ion to electron co-extracted currents in ECR-driven sources [44]. Thus, as **Fig. 9(b)** attests, a ratio of ~0.225 is optimally achieved in H_2 versus ~0.125 in D_2. Additionally, the data of **Fig. 9** disclose that intermediate pressure and power are needed for maximizing this ratio. In **Fig. 9**, the optima are 1.07 Pa/0.4 kW for H_2 and 1.07 Pa/0.3 kW for D_2.

The pressure dependence of the negative ion density and the above ratio is better seen in **Fig. 10**. It is evident that as the pressure increases, a steep negative ion density rise is followed by a quasi-saturation phase; **Fig. 10(a)**. The curves are almost independent of the isotope, in line with the data of **Fig. 8**. Then, the existence of a distinct optimal pressure to enhance the negative ion to cold electron density ratio is shown; **Fig. 10(b)**. This optimum is located at around 1.33 Pa in both discharges (H_2 and D_2). As mentioned above (**Fig. 9**), the H_2 plasma yields a higher value of this ratio.

Finally, a decoupling from the operating parameters and a direct comparison of the negative ion yields in the H_2 and D_2 discharges in terms of endogenous plasma properties, may be attained by plotting the negative ion density versus the plasma density. This is shown in **Fig. 11**. H_2 plasma allows to produce higher negative ion density than D_2 plasma does for a given cold electron density (**Fig. 11(a)**). At the same time, the negative ion densities in the two plasmas are neared when the hot electron density is considered (**Fig. 11(b)**).

IV. Discussion

This section outlines the concept of the ECR heating adopted in this work. Then, in light of the present results, it correlates this concept with the EEDFs, and the production and destruction mechanisms of the H^- and D^- negative ions. These mechanisms refer to dissociative attachment, and associative detachment and mutual neutralization, respectively.

A) ECR heating concept and EEDFs

At the microwave frequency of 2.45 GHz, the magnetic induction required for the ECR condition is 875 x 10^{-4} T. For the ECR modules employed here [41,58], the plasma is produced by electrons accelerated in the region of the

ECR coupling due to the microwave electric field applied via a coaxial line and a permanent magnet at the termination of this line. The trajectories of the electrons in such a multipolar magnetic field have been studied previously [59,60]. In this region, EEDFs appear as the sum of two electron populations. The temperature of the hot electron population can reach more than 17 eV [58]. The plasma is produced by inelastic collisions of these electrons, and it diffuses away from each magnet (see Refs. 1–10 in [41]). Especially for the electrons, in principle hot ones remain trapped in the magnetic field, whereas cold electrons diffuse away from the magnetic field under the influence of density gradients and the resulting space charge electric field [58]. This fact may explain the much lower density (Fig. 3) as well as the almost constant temperature (Fig. 7) of the hot electrons found downstream of the ECR zones, i.e., we probably probe the small fraction of the hot electrons that are capable to escape from the above magnetic filter.

Regarding the isotope effect for the EEDFs shown in Figs. 4 and 5, this may be due both to the different total (i.e., contribution from both dissociative and non-dissociative ionization, in the ECR zones) ionization cross section values for H_2 and D_2, which give an isotope effect near the threshold electron-impact energies [80]. As predicted theoretically, $Q_{ion}^{D_2} > Q_{ion}^{H_2}$ up to 25 eV energy but the cross sections at electron energies larger than 25 eV become equal. Indicative values of the total ionization cross section include $Q_{ion}^{D_2}/Q_{ion}^{H_2} = 1.147$ at 16 eV and $Q_{ion}^{D_2}/Q_{ion}^{H_2} = 1.041$ at 22 eV [80].

Apart from the differences in the ionization cross sections, the ion confinement time in D_2 is $\sqrt{2}$ times higher than in H_2 due to the square root of the mass ratio of the two molecules [13,16], while the positive ions are destroyed by transport to the walls where they are neutralized. Thus, the positive ions are consistently higher in D_2. In other words, the plasma density should be consistently higher in D_2 than in H_2 and their ratio should vary by a factor of about $\sqrt{2}$. **Fig. 12** provides a direct comparison of this plasma density ratio using the values measured in the present work. The ratio approaches but does not precisely equal $\sqrt{2}$, depending on the operating conditions. It indicates that other factors (e.g., the presence of magnetic field, isotope effects in some of the ion-loss cross sections, etc.) may be significant [13,16].

The role of the implied bi-Maxwellian EEDFs in the yield of the H^- and D^- ions is clarified by considering their main production and destruction processes.

B) *Negative ion production reactions and lower energy part of EEDFs*

Table III summarizes the main production processes for the H^- and D^- negative ions. It is generally accepted that the key path for the volume production is the DEA process (reactions R1 and R2), having cross sections as shown in **Figs. 13(a)** and **13(b)** respectively. In both the H_2 and D_2 plasmas, the cross section highly increases as the vibrational level increases and, simultaneously, the (electron) energy threshold of the reaction shifts to lower values. In our case, a direct comparison between EEDFs and DEA cross sections in **Figs. 13(a)** and **13(b)** shows that the cold populations produced in both the H_2 and D_2 plasmas have energies that promote R1 and R2. On the other hand, the DEA cross section is higher in H_2 than in D_2 for every vibrational level and the energy threshold is lower for the same vibrational level.

Fig. 13(c) presents the average H^- and D^- ion densities measured within even spaced intervals of electron temperature. This figure is obtained as follows: for the optimal pressure of 1.07 Pa (see **Fig. 9**), we combine the data of **Figs. 6(b)** and **8(b)** by eliminating the power. Thus, the H^- and D^- ion densities versus the cold electron temperature are obtained as in **Fig. 14**. Then, we average the negative ion densities within 0.1 eV intervals (see grid lines in **Fig. 14**). From the resultant **Fig. 13(c)**, it is deduced that the cold electron temperature that yields negative ions lies between 0.5 and 0.9 eV in H_2 and between 0.7 and 1.1 eV in D_2. According to **Figs. 13(a)** and **13(b)**, these values correspond to the cold electrons that participate to DEA with H_2 and D_2 molecules heated at the vibrational levels $v \geq 7$ and $v \geq 9$, respectively.

However, although it is seen that the higher DEA cross sections and the span of the cold electron temperature in H_2 may favor the negative ion production, this may be partially compensated for the lower cold electron density in the H_2 plasma, compared to the D_2 plasma, as it has been shown in section IVA). This could explain the quite close densities of H^- and D^- ions shown in **Fig. 8** as opposed to the apparent higher H^- ion density in **Fig. 11(a)** where any difference in the cold electron densities has been eliminated. Finally, this concept is in line with the lower ratio of the negative ion to cold electron density, established by **Fig. 9**. Namely, this ratio becomes higher in the H_2 plasma than in the D_2 plasma since the numerator is almost constant whereas the denominator lower by a factor higher than $\sqrt{2}$ (**Fig. 12**). Based on **Fig. 9(b)**, a ratio ~0.225 in H_2 versus ~0.125 in D_2 has been mentioned in section III (at 1.07 Pa and 0.3 to 0.4 kW), i.e., 1.8 times higher in H_2. For the same conditions, **Fig. 12** gives an average cold electron density ~1.77 times higher in the D_2 plasma.

C) *(Ro)vibrational heating and higher energy part of EEDFs*

The present work provides data on the EEDFs but not on the (ro)vibrational heating of the two plasmas. Hence, DEA cross sections and cold electron densities/energies alone, fail to describe the entire DEA process. Direct measurements of the vibrational distribution functions (VDFs) under similar to the present experimental conditions are in progress. Our results in the D_2 plasma have already been published [50], but their correlation with the present results will be realized when the VDFs in H_2 plasma will also be available from our ongoing experiments. However, **Table IV** categorizes the main reactions that lead to the H_2 and D_2 molecules excitation and de-excitation, and they can be correlated with the results of the present work.

Reactions R43 and R44 are recognized as the principal ones, and their cross sections are given in **Figs. 15(a)** and **15(b)**. A direct comparison with **Fig. 7** shows that the hot populations produced in both ECR plasmas have temperatures that lie above the threshold energy of the two reactions. It is repeated that the present measurements refer to the production region of the source, i.e., downstream of the ECR zones, which means that in the ECR zones hot electrons should obtain even higher energies and densities. Thus, H_2 and D_2 gases can be heated vibrationally in the ECR zones efficiently.

Fig. 15(c) compares these cross sections of the reactions R43 and R44 for a given electron energy close to their peak (40 eV) as a function of the final vibrational level. The values of the two cross sections are approaching each other as the vibrational level increases, i.e., at the levels where DEA becomes more efficient; $v \geq 7$ as

discussed in section IVB) for the optimal pressure of 1.07 Pa. Thus, according to section IVB), the interplay between the lower energy part of the EEDFs and the DEA cross sections remains the main reason for the higher negative ion yield in the H_2 plasma than in the D_2 plasma at a given plasma density. In parallel, in both the plasmas, higher hot electron density may lead to higher density of each vibrational level, and thus to higher density of the negative ions. This is probably what makes the linear dependence seen in **Fig. 11(b)**. Nevertheless, the negative ion destruction processes should also be considered.

D) Negative ion destruction reactions

The H^- and D^- negative ion destruction reactions may be direct (**Table III**) or indirect in terms of molecular relaxation (**Table IV**). Among the former, associative detachment (AD: R13, R14) and mutual neutralization (MN: R25–R40) are identified as the dominant ones in the present source [53]. Regarding the molecular relaxation, it is assumed that the V–t process (R51, R52) is the principle one. In further restricting the analysis to the AD and V–t reactions, a simplistic consideration of negative ion destruction may be derived.

Thus, the rates for both reactions are sensitive to the atomic density which depends both on the gas pressure and the injected MW power, while they could be associated with the limitations in the H^- and D^- ion production and as well as with the optima seen in **Figs. 8-10**. In low temperature plasmas, one of the most important electronically inelastic process for the formation of neutral fragments is the excitation of the repulsive $b^3\Sigma_u^+$ state (R57 and R58).

$$e + H_2\left(X^1\Sigma_g^+; v\right) \rightarrow H_2\left(b^3\Sigma_u^+\right) + e \rightarrow 2H + e \qquad \text{R57.}$$

$$e + D_2\left(X^1\Sigma_g^+; v\right) \rightarrow D_2\left(b^3\Sigma_u^+\right) + e \rightarrow 2D + e \qquad \text{R58.}$$

Below about 12 eV, this process is the only mechanism for dissociation of H_2 or D_2 into neutral fragments [81,82] and based on the presents EEDFs (**Figs. 4** and **5**) this process should be active in our source.

In ECR sources [37,38,53] operating with hydrogen, an increase in the atomic density and a decrease in the atomic-to-molecular density for increasing pressure have been reported, whereas the latter was found to increase for increasing power [53]. At the same time, AD and MN reaction rates have been found to increase with hydrogen pressure [53,69]. These findings are consistent with **Fig. 10(a)** where the H^- and D^- ion production is restricted for increasing pressure. The parallel increase of the plasma density (**Fig. 2**) leads to the optima of the ratio in **Fig. 10(b)**.

Finally, regarding the isotope effect between R57 and R58, the atomic-to-molecular density ratio is found to be constantly higher in the case of D_2 plasmas, both by means of experiments [8,28,39] and theoretical analyses [13,33]. In the light of recent calculations [81,82], the cross sections leading from the $v'' = 0$ vibrational level to the ground state display only a small isotope effect. Thus, the commonly observed higher atomic density in D_2 plasmas could be justified by the difference in the transport properties of H and D atoms [83] and points to more

intense AD and MN losses in D_2 plasmas, in agreement with the lower negative ion density for a given plasma density shown in **Fig. 11(a)**.

Conclusions

The present report is devoted to the study of H_2 and D_2 ECR-driven plasmas oriented to negative ion sources. The main claim of the article is the investigation of the isotope effect with respect to main plasma features including the electron energy distribution functions and the negative ion densities. The following statements recap the principal similarities and differences between the H_2 and D_2 plasmas, as they have been ensued from this comparative study. Thus, two electron populations, quasi-Maxwellian, are produced, independently of the gas, the pressure, and the MW power employed. The cold electron population is constantly higher in the D_2 plasma, and this is attribute to the higher confinement time of positive ions in the case of deuterium. H^- and D^- negative ion densities are not substantially different in the two plasmas under the same operating conditions, although the H^- negative ion yield is higher for a given plasma density. A strong isotope effect exists when the negative ion to electron density ratio is considered, and the latter may be up to 80% higher in the H_2 plasma. H^- and D^- negative ions are produced in the plasma volume through dissociative attachment of cold electrons onto vibrationally excited molecules. Finally, similar optimal operational windows for enhanced negative ion yield do exist in both gases, as a compromise between production and destruction processes.

Acknowledgements

- The present work was funded by the "Andreas Mentzelopoulos" PhD scholarships of the University of Patras (M. M.).
- This work has been carried out within the framework of the EUROfusion Consortium, funded by the European Union via the Euratom Research and Training Programme (Grant Agreement No 101052200 — EUROfusion). Views and opinions expressed are however those of the author(s) only and do not necessarily reflect those of the European Union or the European Commission. Neither the European Union nor the European Commission can be held responsible for them. The authors are grateful to Dr M. Bacal for enlightening discussions.

References

[1] R. Hemsworth, H. Decamps, J. Graceffa, B. Schunke, M. Tanaka, M. Dremel, A. Tanga, H.P.L De Esch, F. Geli, J. Milnes, T. Inoue, D. Marcuzzi, P. Sonato and P. Zaccaria, "Status of the ITER heating neutral beam system", Nucl. Fusion **49**, 045006 (2009).

[2] R. S. Hemsworth, D. Boilson, P. Blatchford, M. Dalla Palma, G. Chitarin, H. P. L. De Esch, F. Geli, M. Dremel, J. Graceffa, D. Marcuzzi, G. Serianni, D. Shah, M. Singh, M. Urbani, P. Zaccaria, "Overview of the design of the ITER heating neutral beam injectors", New. J. Phys. **19**, 025005 (2017).

[3] R. S. Hemsworth and T. Inoue, "Positive and Negative Ion Sources for Magnetic Fusion", IEEE Trans. Plasma Sci. **33**(6), 1799 (2005).

[4] B. Schunke, D. Boilson, J. Chareyre, C.-H. Choi, H. Decamps, A. El-Ouazzani, F. Geli, J. Graceffa, R. Hemsworth, M. Kushwah, K. Roux, D. Shah, M. Singh, L. Svensson and M. Urbani, "Overview of the negative ion based neutral beam injectors for ITER", Rev. Sci. Instrum. **87**, 02C101 (2016).

[5] B. Heinemann, U. Fantz, W. Kraus, L. Schiesko, C. Wimmer, D. Wünderlich, F. Bonomo, M. Fröschle, R. Nocentini, R. Riedl, "Towards large and powerful radio frequency driven negative ion sources for fusion", New J. Phys. **19**, 015001 (2017).

[6] U. Fantz, P. Franzen, W. Kraus, H. D. Falter, M. Berger, S. Christ-Koch, M. Fröschle, R. Gutser, B. Heinemann, C. Martens, P. McNeely, R. Reidl, E. Speth and D. Wünderlich, "Low pressure and high power rf sources for negative hydrogen ions for fusion applications (ITER neutral beam injection) (invited)", Rev. Sci. Instrum. **79**, 02A511 (2008).

[7] S. Christ-Koch, U. Fantz, M. Berger, NNBI Team, "Laser photodetachment on a high power, low pressure rf–driven negative hydrogen ion source", Plasma Sources Sci. Technol. **18**, 025003 (2009).

[8] U. Fantz, L. Schiesko, D. Wünderlich, NNBI Team, "A Comparison Of Hydrogen And Deuterium Plasmas In The IPP Prototype Ion Source For Fusion", AIP Conf. Proc. **1515**, 187-196 (2013).

[9] M. Bacal, M. Wada, "Negative hydrogen ion production mechanisms", Appl. Phys. Rev. **2**, 021305 (2015).

[10] D. Wünderlich, R. Riedl, I. Mano, A. Mimo, U. Fantz, B. Heinemann, W. Kraus, "Formation of large negative deuterium ion beams at ELISE", Rev. Sci. Instrum. **90**, 113304 (2019).

[11] W. Kraus, D. Wünderlich, U. Fantz, B. Heinemann, F. Bonomo and R. Reidl, "Deuterium results at the negative ion source test facility ELISE", Rev. Sci. Instrum. **89**, 052102 (2018).

[12] G. Serianni, V. Toigo, M. Bigi, G. Chitarin, S. Dal Bello, L. Grando, A. Luchetta, D. Marcuzzi, R. Pasqualotto, N. Pomaro, P. Zaccaria, L. Zanotto, P. Agostinetti, M. Agostini, V. Antoni, D. Aprile, M. Barbisan, M. Battistella, M. Brombin, R. Cavazzana, M. Dalla Palma, M. Dan, A. De Lorenzi, R. Delogu, M. De Muri, S. Denizeau, M. Fadone, F. Fellin, L. Ferbel, A. Ferro, E. Gaio, G. Gambetta, F. Gasparini, F. Gnesotto, P. Jain, A. Maistrello, G. Manduchi, S. Manfrin, G. Marchiori, N. Marconato, M. Moresco, T. Patton, M. Pavei, S. Peruzzo, N. Pilan, A. Pimazzoni, R. Piovan, C. Poggi, M. Recchia, A. Rizzolo, G. Rostagni, E. Sartori, M. Siragusa, P. Sonato, E. Spada, S. Spagnolo, M. Spolaore, C. Taliercio, P. Tinti, M. Ugoletti, M. Valente, A. Zamengo, B. Zaniol, M. Zaupa, C. Baltador, M. Cavenago, D. Boilson, C. Rotti, P. Veltri, T. Bonicelli, F. Paolucci, S. Muriel, A. Masiello,

A. Chakraborty, H. Patel, N. P. Singh, U. Fantz, B. Heinemann, W. Kraus, M. Kashiwagi, K. Tsumori, "SPIDER in the roadmap of the ITER neutral beams", Fusion Eng. Des. **146**, 2539 (2019).

[13] D. A. Skinner, A. M. Bruneteau, P. Berlemont, C. Courteille, R. Leroy and M. Bacal, "Isotope effect and electron-temperature in volume H^- and D^- ion sources", Phys. Rev. E **48**(3), 2122 (1993).

[14] A. M. Bruneteau, C. Courteille, R. Leroy and M. Bacal, "Investigation of two negative hydrogen and deuterium ion sources: Effect of the volume", Rev. Sci. Instrum. **67**(11), 3827-3830 (1996).

[15] A. A. Mullan and W. G. Graham, "Plasma parameter characterization of a tandem multicusp ion source operating in H_2 and D_2", Rev. Sci. Instrum. **61**(1), 451 (1990).

[16] A. A. Mullan and W. G. Graham, "Study of the discharge of a multicusp ion source operating with H_2 and D_2", J. Phys. D: Appl. Phys. **24**, 1533 (1991).

[17] R. Leroy, M. Bacal, P. Berlemont, C. Courteille and R. A. Stern, "H^- and D^- temperature in volume sources", Rev. Sci. Instrum. **63**(4), 2686 (1992).

[18] O. Fukumasa, S. Mori, "Volume production of D^- negative ions in low-pressure D_2 plasmas – negative ion densities versus plasma parameters", Nucl. Fusion **46**, S287 – S296 (2006).

[19] S. Mori, O. Fukumasa, "D^-/H^- negative ion production versus plasma parameters in a volume negative ion source", Rev. Sci. Instrum. **79**, 02A507 (2008).

[20] T. Inoue, G. D. Ackerman, W. S. Cooper, M. Hanada, J. W. Kwan, Y. Ohara, "Comparison of H^- and D^- production in a magnetically filtered multicusp source", Rev. Sci. Instrum. **61**(1), 496 (1990).

[21] R. McAdams, R. F. King, A. F. Newman, "Hydrogen/deuterium negative ion scaling from a magnetic multipole ion source", Rev. Sci. Instrum. **63**(2), 1777 (1992).

[22] M. Hamabe, Y. Oka, M. Osakabe, Y. Takeiri, K. Tsumori, O. Kaneko, "Comparison of H^-/D^- measurement in the magnetically filtered region of the large negative ion source", Rev. Sci. Instrum. **71**(2), 1151 (2000).

[23] K. Ikeda, K. Tsumori, H. Nakano, M. Kisaki, N. Nagaoka, S. Kamio, Y.Fujiwara, Y. Haba, M. Osakabe, "Exploring deuterium beam operation and the behavior of the co–extracted electron current in a negative–ion–based neutral beam injector", Nucl. Fusion **59**, 076009 (2019).

[24] M. Bacal, C. Michaut, L. I. Elizarov and F. El Balghiti, "Basic processes of negative ion production and destruction in sources and beams (invited)", Rev. Sci. Instrum. **67**(3), 1138-1143 (1996).

[25] C. Jacquot, J. Pamela, D. Riz, Yu. Belchenko, "Negative ion production in large volume source with small deposition of cesium", Rev. Sci. Instrum. **67**(3), 1036 (1996).

[26] R. McAdams, R. F. King, G. Proudfoot, A. J. T. Holmes, "Pure and cesiated CW volume source performance at the Culham ion source test stand", AIP Conf. Proc. **287**, 353 (1994).

[27] J. Komppula, O. Tarvainen, T. Kalvas, H. Koivisto, P. Myllyperkiö, V. Toivanen, "A study of VUV emission and the extracted electron–ion ratio in hydrogen and deuterium plasmas of a filament-driven H^-/D^- ion source", Phys. Plasmas **26**, 073517 (2019).

[28] D. Rauner, S. Briefi, U. Fantz, "RF power transfer efficiency of inductively coupled low pressure H_2 and D_2 discharges", Plasma Sources Sci. Technol. **26**, 095004 (2017).

[29] S. Christofaro, R. Friedl, U. Fantz, "Negative Hydrogen and Deuterium Ion Density in a Low Pressure Plasma in Front of a Converter Surface at Different Work Functions", Plasma **4**, 94 (2021).

[30] L. Schiesko, M. Carrère, J–M. Layet, G. Cartry, "A comparative study of H^- and D^- production on graphite surfaces in H_2 and D_2 plasmas", Plasma Sources Sci. Technol. **19**, 045016 (2010).

[31] G. Cartry, D. Kogut, K. Achkasov, J–M. Layet, T. Farley, A. Gicquel, J. Achard, O. Brinza, T. Bieber, H. Khemliche, P. Roncin, A. Simonin, "Alternative solutions to ceasium in negative–ion sources: a study of negative–ion surface production on diamond in H_2/D_2 plasmas", New J. Phys. **19**, 025010 (2017).

[32] S, Briefi, U. Fantz, "Investigation of helicon discharges as RF coupling concept of negative hydrogen ion sources", AIP. Conf. Proc. **1515**, 278-283 (2013).

[33] C. Marini, R. Agnello, B. P. Duval, I. Furno, A. A. Howling, R. Jacquier, A. N. Karpushov, G. Plyushchev, K. Verhaegh, Ph. Guitienne, U. Fantz, D. Wünderlich, S. Béchu, A. Simonin, "Spectroscopic characterization of H_2 and D_2 helicon plasmas generated by a resonant antenna for neutral beam applications in fusion", Nucl. Fusion **57**, 036024 (2017).

[34] R. Agnello, S. Béchu, I. Furno, Ph. Guittienne, A. A. Howling, R. Jacquier, G. Plyushchev, M. Barbisan, R. Pasqualotto, I. Morgal and A. Simonin, "Negative ion characterization in a helicon plasma source for fusion neutral beams by cavity ring–down spectroscopy and Langmuir probe laser photodetachment", Nucl. Fusion **60**, 026007 (2020).

[35] V. D. Dougar-Jabon, "Production of Hydrogen and Deuterium Negative Ions in an Electron Cyclotron Resonance Driven Plasma", Physica Scripta **63**, 322-325 (2001).

[36] V. D. Dougar Jabon, A. J. Chacon Velasco, F. A. Vivas, "Hydrogen negative ion production in an electron cyclotron resonance driven plasma", Rev. Sci. Instrum. **69**(2), 950 (1998).

[37] D. Rauner, U. Kurutz and U. Fantz, "Comparison of Measured and Modelled Negative Hydrogen Ion Densities at the ECR-Discharge HOMER", AIP Conf. Proc. **1655**, 020017 (2015).

[38] R. Friedl, D. Rauner, A. Heiler and U. Fantz, "Dissociative recombination and its impact on the line profile of the hydrogen Balmer series", Plasma Sources Sci. Technol. **29**, 015014 (2020).

[39] R. Friedl, U. Kurutz, U. Fantz, "Efficiency of Cs–free Materials for Negative Ion Production in H_2 and D_2 Plasmas", AIP Conf. Proc. 1869, 030022 (2016).

[40] U. Kurutz, R. Friedl and U. Fantz, "Investigations on Cs–free alternatives for negative ion formation in a low pressure hydrogen discharge at ion source relevant parameters", Plasma Phys. Control. Fusion **59**, 075008 (2017).

[41] A. Lacoste, T. Lagarde, S. Béchu, Y. Arnal, J. Pelletier, "Multi-dipolar plasmas for uniform processing: physics, design and performance", Plasma Sources Sci. Technol. **11**, 407-412 (2002).

[42] A. A. Ivanov, Jr., C. Rouillé, M. Bacal, Y. Arnal, S. Béchu and J. Pelletier, "H^- ion production in electron cyclotron resonance driven multicusp volume source", Rev. Sci. Instrum. **75**(5), 1750 (2004).

[43] P. Svarnas, J. Breton, M. Bacal, and T. Mosbach, "Pressure optimization for H^- ion production in an electron cyclotron resonance-driven and a filamented source", Rev. Sci. Instrum. **77**, 03A532 (2006).

[44] P. Svarnas, J. Breton, M. Bacal, R. Faulkner, "Plasma Electrode Bias Effect on the H^- Negative–Ion Density in an Electron Cyclotron Resonance Volume Source", IEEE Trans. Plasma Sci. **35**(4), 1156 (2007).

[45] P. Svarnas, B. M. Annaratone, S. Béchu, J. Pelletier, M. Bacal, "Study of hydrogen plasma in the negative–ion extraction region", Plasma Sources Sci. Technol. **18**, 045010 (2009).

[46] S. Béchu, A. Soum-Glaude, A. Bès, A. Lacoste, P. Svarnas, S. Aleiferis, A. A. Ivanov and M. Bacal, "Multi–dipolar microwave plasmas and their application to negative ion production", Phys. Plasmas **20**, 101601 (2013).

[47] S. Aleiferis, "Experimental study of H^- negative ion production by electron cyclotron resonance plasmas", Electrical and Computer Engineering Department, University of Patras, Doctoral Thesis No. 350 (2017).

[48] J. Bentounes, S. Béchu, F. Biggins, A. Michau, L. Gavilan, J. Menu, L. Bonny, D. Fombaron, A. Bès, Yu. A. Lebedev, V. A. Shakhatov, P. Svarnas, T. Hassaine, J. L. Lemaire, A. Lacoste, "Effects of the plasma–facing materials on the negative ion H^- density in an ECR (2.45 GHz) plasma", Plasma Sources Sci. Technol. **27**, 055015 (2018).

[49] S. Béchu, S. Aleiferis, J. Bentounes, L. Gavilan, V. A. Shakhatov, A. Bès, P. Svarnas, S. Mazouffre, N. de Oliviera, R. Engeln and J. L. Lemaire, "Detection of rovibrationally excited molecular hydrogen in the electronic ground state via synchrotron radiation", Appl. Phys. Lett. **111**, 074103 (2017).

[50] S. Béchu, J. L. Lemaire, L. Gavilan, S. Aleiferis, V. Shakhatov, Yu. A. Lebedev, D. Fombaron, L. Bonny, J. Menu, A. Bès, P. Svarnas, N. de Oliviera, "Direct measurements of electronic ground state ro-vibrationally excited D_2 molecules produced on ECR plasma-facing materials by means of VUV-FT spectroscopy", J. Quant. Spectrosc. Radiat. Transf. **257**, 107325 (2020).

[51] S. Aleiferis, P. Svarnas, I. Tsiroudis, S. Béchu, M. Bacal, A. Lacoste, "H^- Negative Ion Production From a 2D Network of ECR Dipolar Plasma Sources", IEEE Trans. Plasma Sci. **42**(10), 2828 (2014).

[52] S. Aleiferis, O. Tarvainen, P. Svarnas, M. Bacal, S. Béchu, "Experimental investigation of the relation between H^- negative ion density and Lyman–α emission intensity in a microwave discharge", J. Phys. D: Appl. Phys. 49, 095203 (2016).

[53] S. Aleiferis, P. Svarnas, S. Béchu, O. Tarvainen and M. Bacal, "Production of hydrogen negative ions in an ECR volume source: balance between vibrational excitation and ionization", Plasma Sources Sci. Technol. **27**, 075015 (2018).

[54] R. Behrisch, J. Ehrenberg, M. Wielunski, A. P. Martinelli, H. Bergsåker, B. Emmoth, L. De Kock, J. P. Coad, "Hydrogen and Deuterium retention in wall samples of JET", J. Nucl. Mater. **145–147**, 723–726 (1987).

[55] S. Aleiferis and P. Svarnas, "Automated electrostatic probe device of high resolution and accuracy", Rev. Sci. Instrum. **85**, 123504 (2014).

[56] M. Bacal, "Photodetachment diagnostic techniques for measuring negative ion densities and temperatures in plasmas", Rev. Sci. Instrum. **71**(11), 3981 (2000).

[57] P. M. Bryant, J. W. Bradley, "Optimum circuit design for the detection of laser photodetachment signals", Plasma Sources Sci. Technol. **22**, 015014 (2013).

[58] T. Lagarde, Y. Arnal, A. Lacoste, J. Pelletier, "Determination of the EEDF by Langmuir probe diagnostics in a plasma excited at ECR above a multipolar magnetic field", Plasma Sources Sci. Technol. **10**, 181-190 (2001).

[59] J. Pelletier, "Distributed ECR Plasma Sources *High Density Plasma Sources: Design, Physics and Performance*", ed O. A. Popov (Park Ridge, NJ: Noyes) pp 380–425 (1995).

[60] J. Pelletier, G. Matthieussent, "Homogeneity in multipolar discharges: the role of primary electrons *Microwave Excited Plasmas*", ed M. Moisan and J. Pelletier (Amsterdam: Elsevier) pp 351-384 (1992).

[61] J. N. Bardsley, J. M. Wadehra, "Dissociative attachment and vibrational excitation in low-energy collisions of electrons with H_2 and D_2", Phys. Rev. A **20**(4), 1398 (1979).

[62] R. Celiberto, R. K. Janev, A. Laricchiuta, M. Capitelli, J. M. Wadehra, D. E. Atems, "Cross section data for electron–impact inelastic processes of vibrationally excited molecules of hydrogen and its isotopes", At. Data Nucl. Data Tables **77**, 161 (2001).

[63] M. Bacal and M. Wada, "Negative ion source operation with deuterium", Plasma Sources Sci. Technol. **29**, 033001 (2020).

[64] B. Peart, K. T. Dolder, "Collision between electrons and H_2^+ ions VI. Measurements of cross sections for the simultaneous production of H^+ and H^-", J. Phys. B: Atom. Molec. Phys. **8**(9), 1570 (1975).

[65] B. Peart, K. T. Dolder, "Measurements of cross sections for the dissociative recombination of D_2^+ ions", J. Phys. B: Atom. Molec. Phys. **6**, L359 (1973).

[66] K. A. Miller, H. Bruhns, M. Čížek, J. Eliášek, R. Cabrera-Trujillo, H. Kreckel, A. P. O'Connor, X. Urbain, D. W. Savin, "Isotope effect for associative detachment: $H(D)^- + H(D) \rightarrow H_2(D_2) + e^-$", Phys. Rev. A **86**, 032714 (2012).

[67] W. G. Graham, "The kinetics of negative hydrogen ions in discharges", Plasma Sources Sci. Technol. **4**, 281–292 (1995).

[68] R. K. Janev, D. Reiter, U. Samm, "Collision Processes in Low-Temperature Hydrogen Plasma", Forschungszentrum, Zentralbibliothek (2003).

[69] W. Yang, S. N. Averkin, A. V. Khrabrov, I. D. Kaganovich, Y–N. Wang, S. Aleiferis, P. Svarnas, "Benchmarking and validation of global model code for negative hydrogen ion sources", Phys. Plasmas **25**, 113509 (2018).

[70] A. V. Dem'yanov, N. A. Dyatko, I. V. Kochetkov, A. P. Napartovich, A. F. Pal', V. V. Pichugin, A. N. Starostin, "Properties of a beam–driven discharge in an H_2-Ar mixture", Sov. J. Plasma Phys. **11**(3), 210 (1985).

[71] M. S. Huq, L. D. Doverspike, R. L. Champion, "Electron detachment for collisions of H^- and D^- with hydrogen molecules", Phys. Rev. A. **27**(6), 2831 (1983).

[72] M. J. J. Eerden, M. C. M. van de Sanden, D. K. Otorbaev, D. C. Schram, "Cross section for the mutual neutralization reaction $H_2^+ + H^-$, calculated in a multiple–crossing Landau–Zener approximation", Phys. Rev. A. **51**(4), 3362 (1995).

[73] A. A. Matveyev, V. P. Silakov, "Kinetic processes in a highly–ionized non–equilibrium hydrogen plasma", Plasma Sources Sci. Technol. **4**, 606–617 (1995).

[74] M. Capitelli, M. Cacciatore, R. Celiberto, O. De Pascale, P. Diomede, F. Esposito, A. Gicquel, C. Gorse, K. Hassouni, A. Laricchiuta, S. Longo, D. Pagano, M. Rutigliano, "Vibrational kinetics, electron dynamics and elementary processes in H_2 and D_2 plasmas for negative ion production: modelling aspects", Nucl. Fusion **46**, S260–S274 (2006).

[75] S. Morisset, F. Aguillon, M. Sizun, V. Sidis, "Quantum dynamics of H_2 formation on a graphite surface through the Langmuir Hinshelwood mechanism", J. Chem. Phys. **121**, 6493 (2004).

[76] D. D. Eley, E. K. Rideal, Parahydrogen conversion on Tungsten, Nature **146**, 401 (1940).

[77] J. Harris, B. Kasemo, "On precursor mechanisms for surface reactions", Surface Science **105**, L281–L287 (1981).

[78] B. Gordiets, C. M. Ferreira, M. J. Pinheiro, A. Ricard, "Self–consistent kinetic model of low–pressure N_2-H_2 flowing discharges: I. Volume processes", Plasma Sources Sci. Technol. **7**, 363–378 (1998).

[79] J. R. Hiskes, A. M. Karo, "Analysis of the vibrational distribution in a hydrogen discharge", Appl. Phys. Lett. **54**(6), 508 (1989).

[80] J.-S. Yoon, Y.-W. Kim, D.-C. Kwon, M.-Y. Song, W.-S. Chang, C.-G. Kim, V. Kumar, B. Lee, "Electron–impact cross sections for deuterated hydrogen and deuterium molecules", Rep. Prog. Phys. **73**, 116401 (2010).

[81] L. H. Scarlett, D. V. Fursa, J. Knol, M. C. Zammit, I. Bray, "Isotopic and vibrational-level dependence of H_2 dissociation by electron impact", Phys. Rev. A. **103**, L020801 (2021).

[82] L. H. Scarlett, D. V. Fursa, M. C. Zammit, I. Bray, Y. Ralchenko, "Complete collision data set for electrons scattering on molecular hydrogen and its isotopologues: II. Fully vibrationally-resolved electronic excitation of the isotopologues of $H_2\left(X^1\Sigma_g^+\right)$", At. Data Nucl. Data Tables **139**, 101403 (2021).

[83] X. Yang, D. Kogut, L. Couëdel, T. Angot, P. Roubin, J.-B. Faure, G. Cartry, "TALIF measurements of hydrogen and deuterium surface loss probabilities on quartz in low pressure high density plasmas", Plasma Sources Sci. Technol. **30**, 015013 (2021).

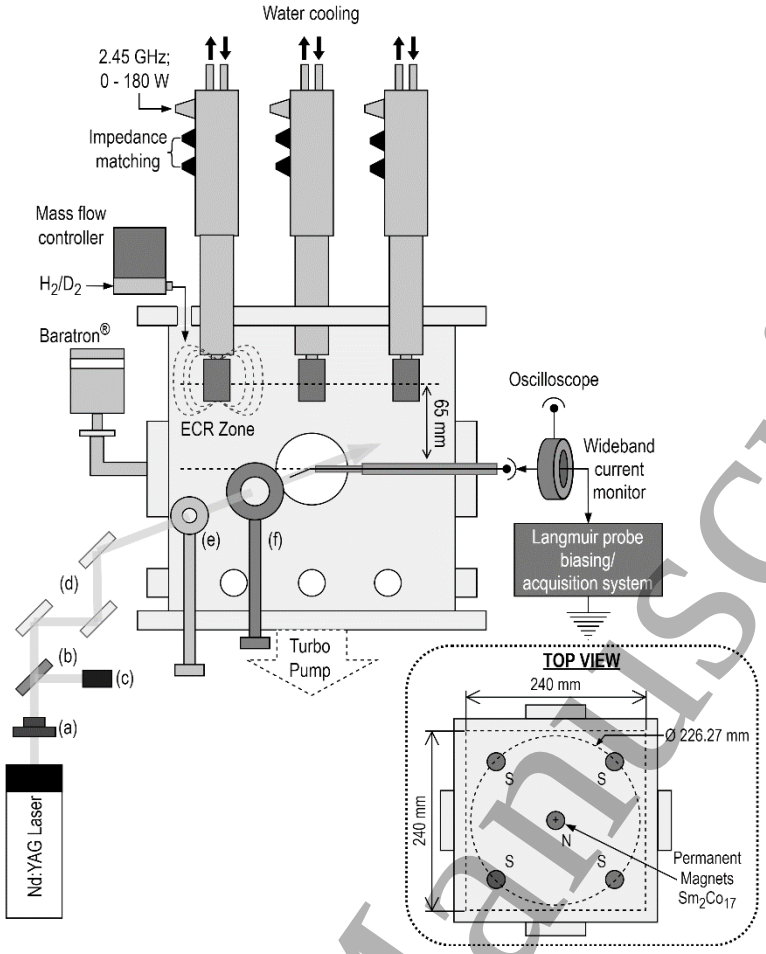

Figure 1. Conceptual design of the experimental setup depicting the ECR–driven source Prometheus I and the diagnostics installed for the present work (electrostatic probe and laser photo-detachment). (a) half wave plate on a precision rotation mount; (b) beam splitter; (c) laser beam dump; (d) mirrors; (e) Ø5 mm cylindrical diaphragm; (f) pyroelectric laser energy sensor (removable). The inset depicts the distribution of the ECR modules.

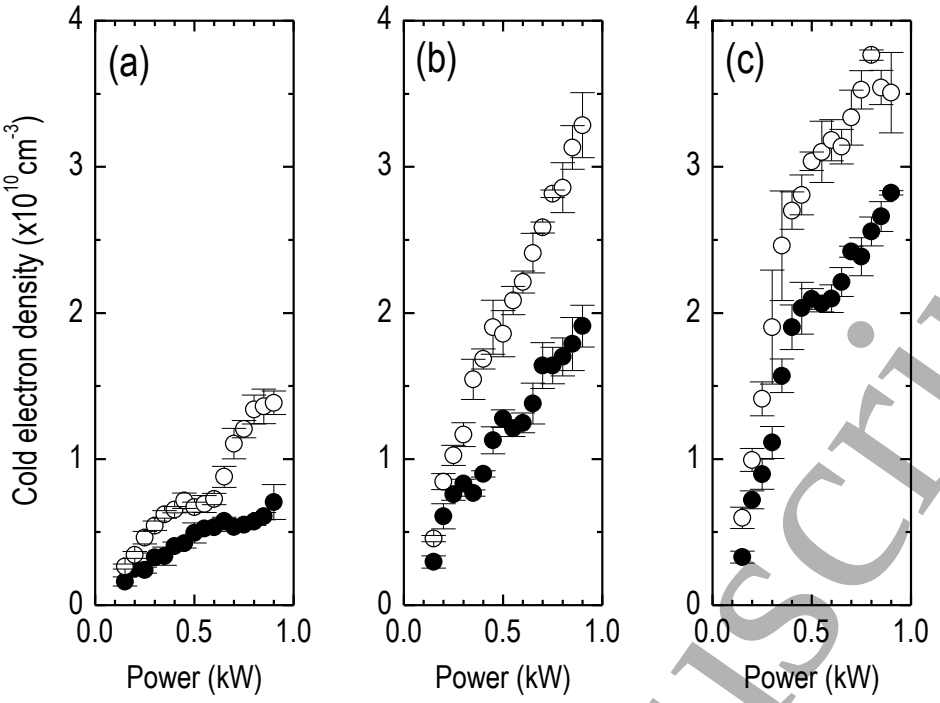

Figure 2. Cold electron density as a function of the MW power at **(a)** 0.53 Pa, **(b)** 1.07 Pa, and **(c)** 1.60 Pa. Solid circles: H_2 plasma. Open circles: D_2 plasma. Mean values and standard deviations are derived from four series of experiments (2 sets on 2 different dates).

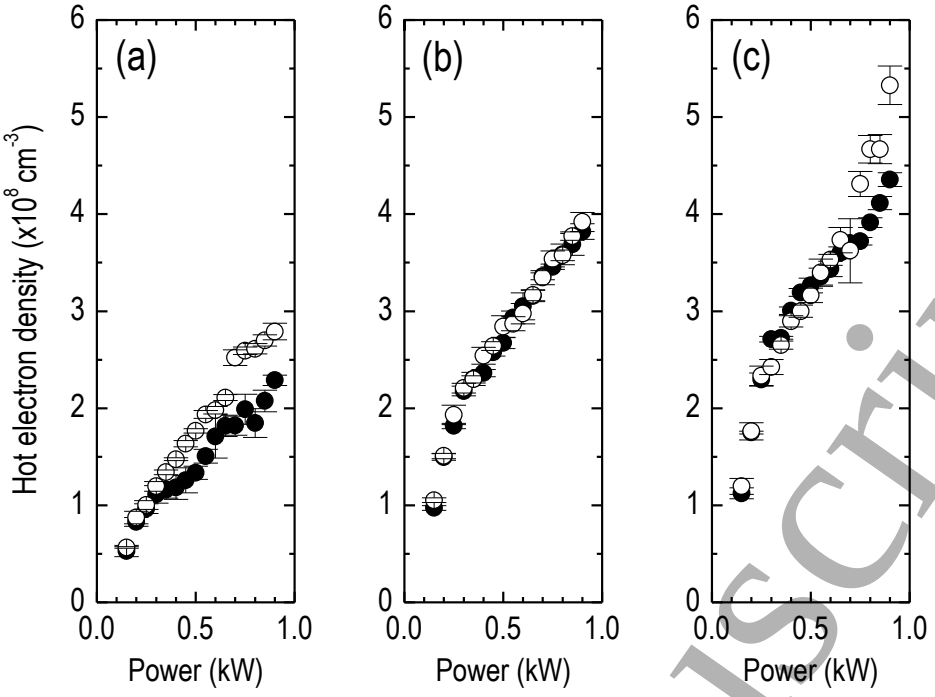

Figure 3. Hot electron density as a function of the MW power at **(a)** 0.53 Pa, **(b)** 1.07 Pa, and **(c)** 1.60 Pa. Solid circles: H_2 plasma. Open circles: D_2 plasma. Mean values and standard deviations are derived from four series of experiments (2 sets on 2 different dates).

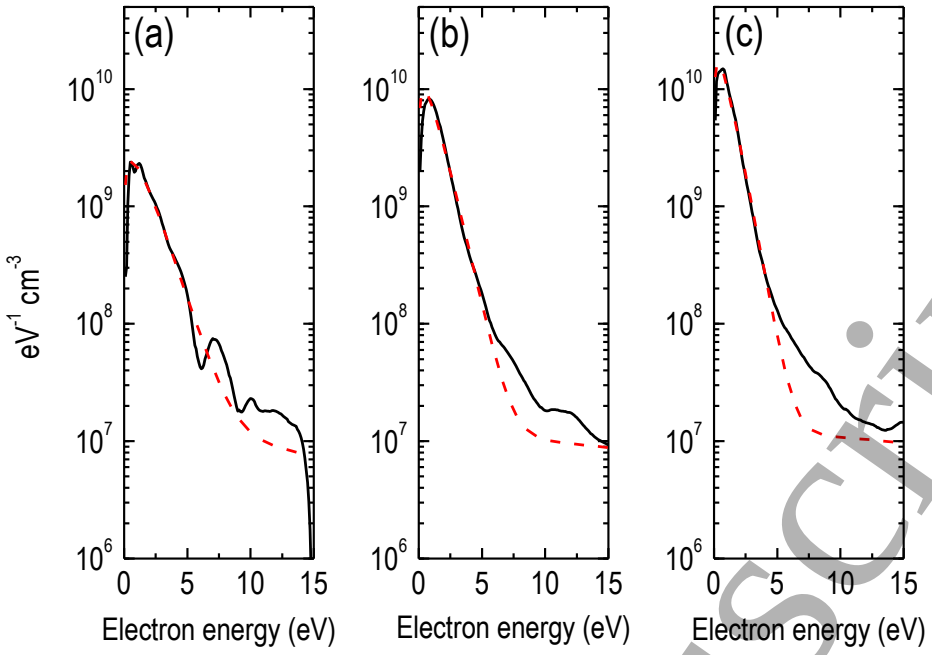

Figure 4. Representative EEDFs from the H_2 ECR plasmas. **(a)** 0.53 Pa; 0.75 kW. **(b)** 1.07 Pa; 0.75 kW. **(c)** 1.60 Pa; 0.75 kW. Solid-black lines: Druyvesteyn method. Dashed-red lines: bi-Maxwellian assumption.

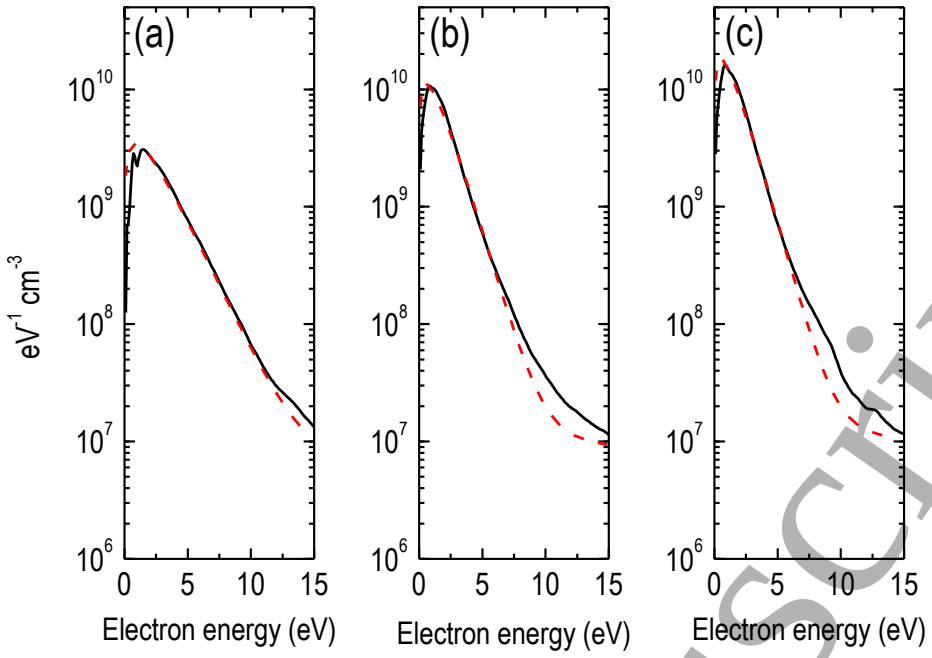

Figure 5. Representative EEDFs from the D_2 ECR plasmas. **(a)** 0.53 Pa; 0.75 kW. **(b)** 1.07 Pa; 0.75 kW. **(c)** 1.60 Pa; 0.75 kW. Solid-black lines: Druyvesteyn method. Dashed-red lines: bi-Maxwellian assumption.

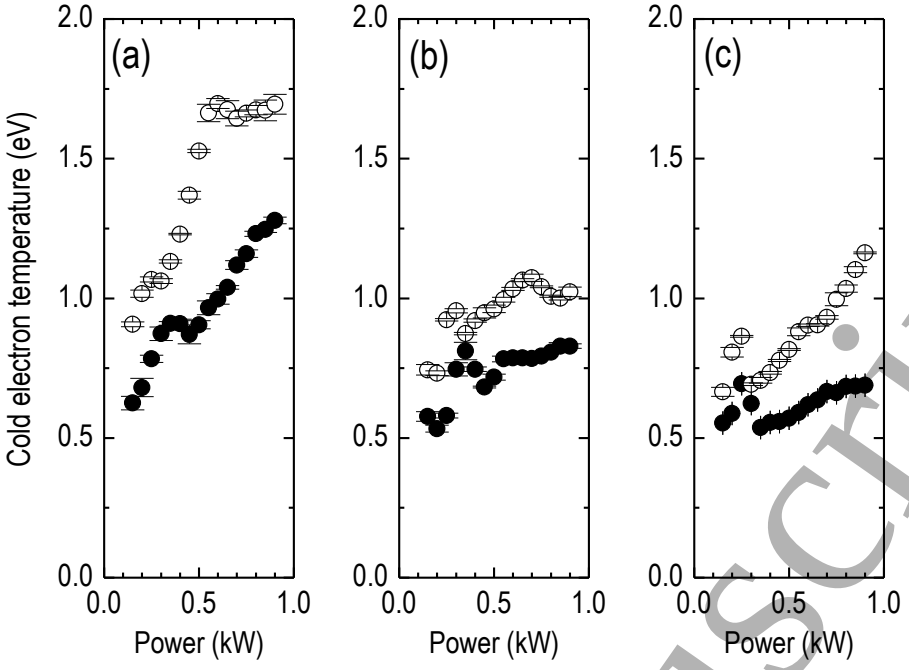

Figure 6. Cold electron temperature as a function of the MW power at **(a)** 0.53 Pa, **(b)** 1.07 Pa, and **(c)** 1.60 Pa. Solid circles: H_2 plasma. Open circles: D_2 plasma. Mean values and standard deviations are derived from four series of experiments (2 sets on 2 different dates).

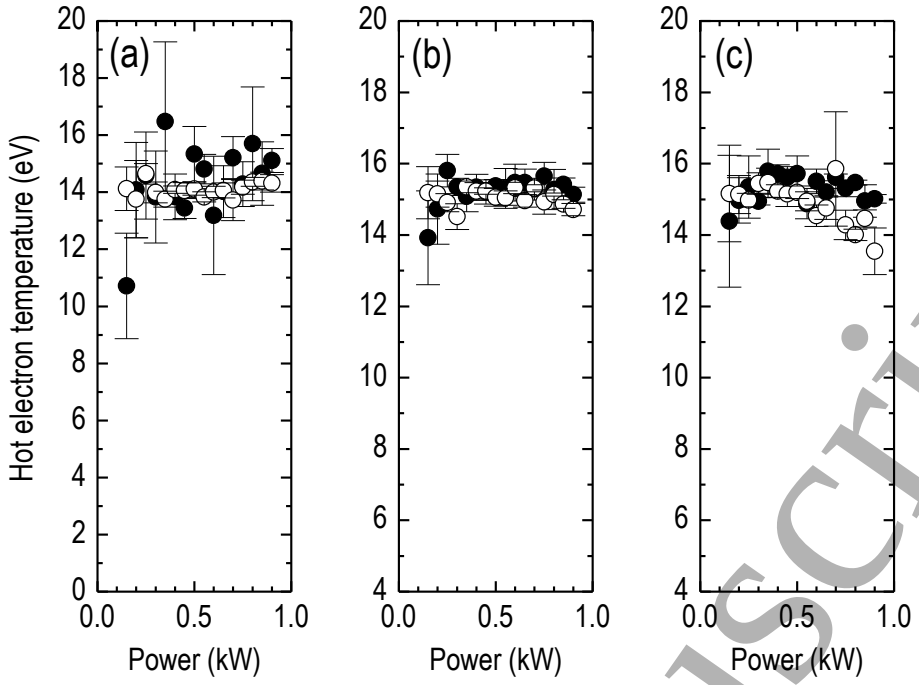

Figure 7. Hot electron temperature as a function of the MW power at **(a)** 0.53 Pa, **(b)** 1.07 Pa, and **(c)** 1.60 Pa. Solid circles: H_2 plasma. Open circles: D_2 plasma. Mean values and standard deviations are derived from four series of experiments (2 sets at 2 different dates).

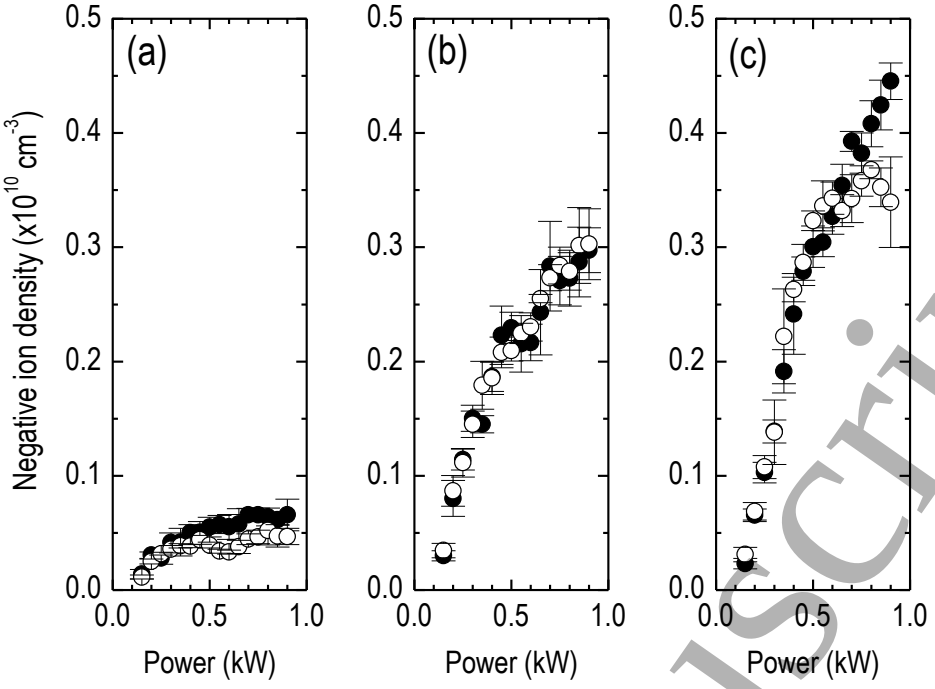

Figure 8. Negative ion density as a function of the MW power at **(a)** 0.53 Pa, **(b)** 1.07 Pa, and **(c)** 1.60 Pa. Solid circles: H_2 plasma. Open circles: D_2 plasma. Mean values and standard deviations are derived from four series of experiments (2 sets on 2 different dates).

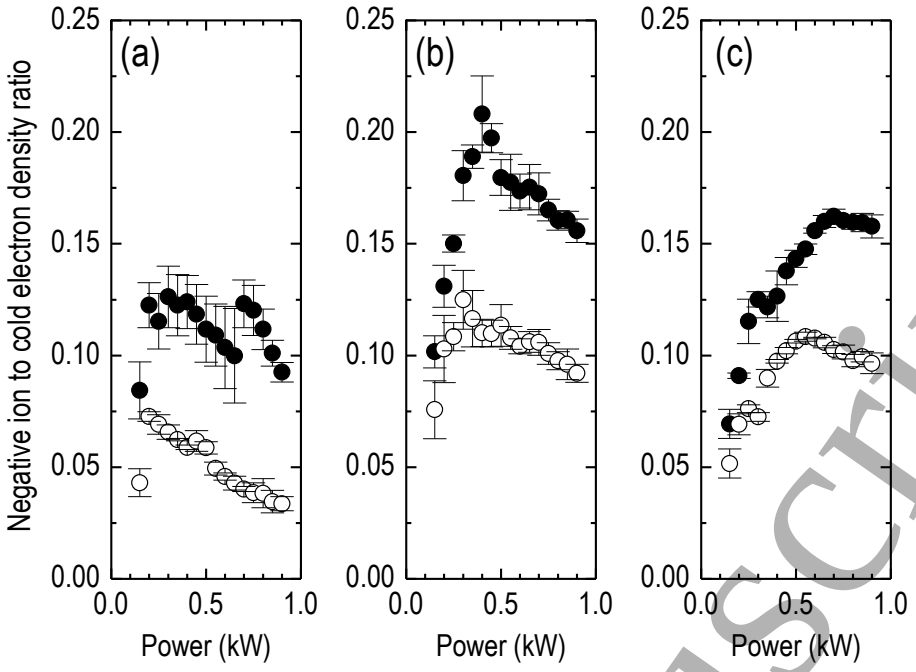

Figure 9. Negative ion to cold electron density as a function of the MW power at **(a)** 0.53 Pa, **(b)** 1.07 Pa, and **(c)** 1.60 Pa. Solid circles: H_2 plasma. Open circles: D_2 plasma. Mean values and standard deviations are derived from four series of experiments (2 sets on 2 different dates).

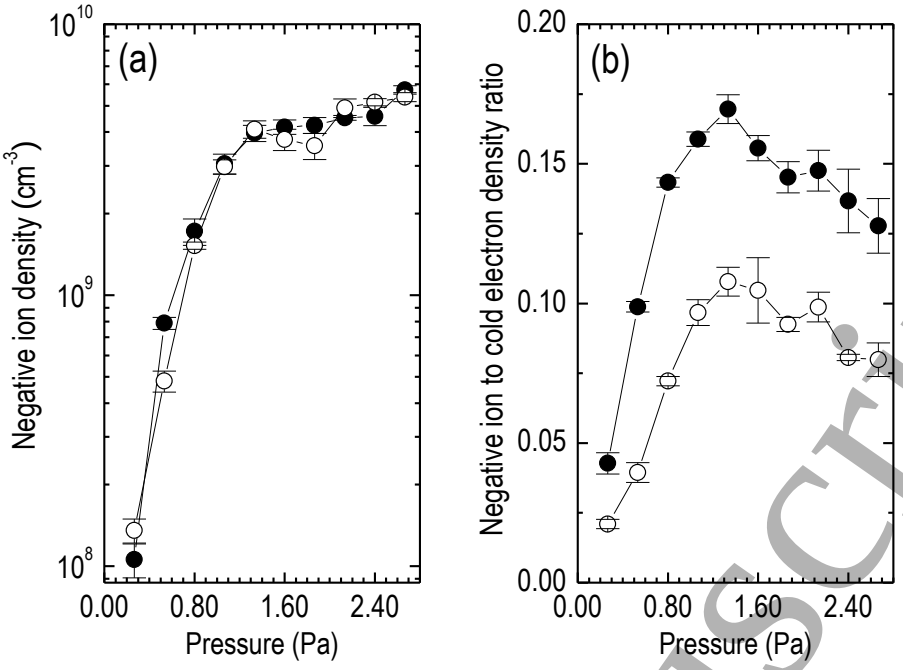

Figure 10. (a) Negative ion density and **(b)** Negative ion to cold electron density, as a function of the working pressure (0.9 kW). Solid circles: H_2 plasma. Open circles: D_2 plasma. Mean values and standard deviations are derived from four series of experiments (2 sets on 2 different dates).

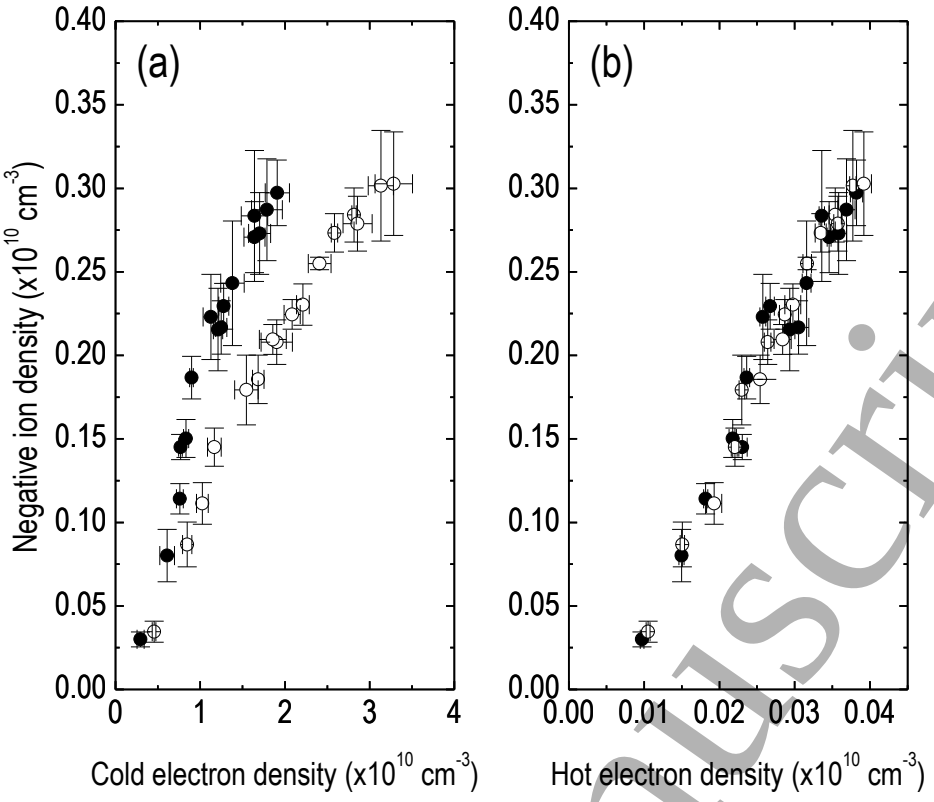

Figure 11. Negative ion density as a function of the density of the: **(a)** cold electron population, **(b)** hot electron population. Solid circles: H_2 plasma. Open circles: D_2 plasma. Mean values and standard deviations are derived from four series of experiments (2 sets at 2 different dates). 1.07 Pa.

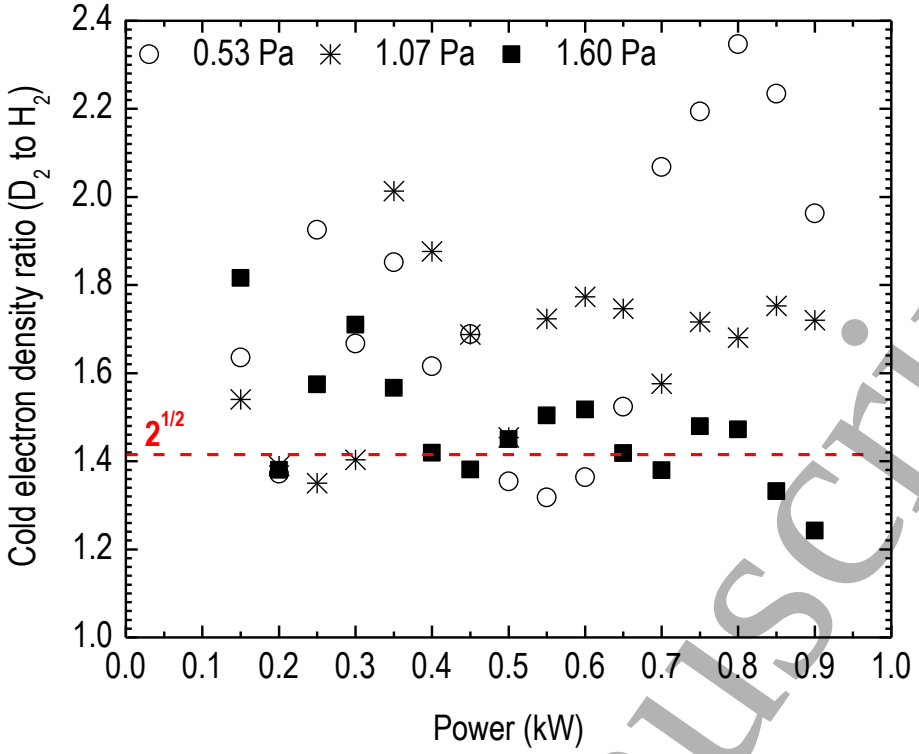

Figure 12. Ratio of the cold electron densities measured in the D_2 plasma to the cold electron densities measured in the H_2 plasma, from Fig. 2, as a function of the MW power at three different pressures. The level of $\sqrt{2}$ is given for comparison reasons; see text.

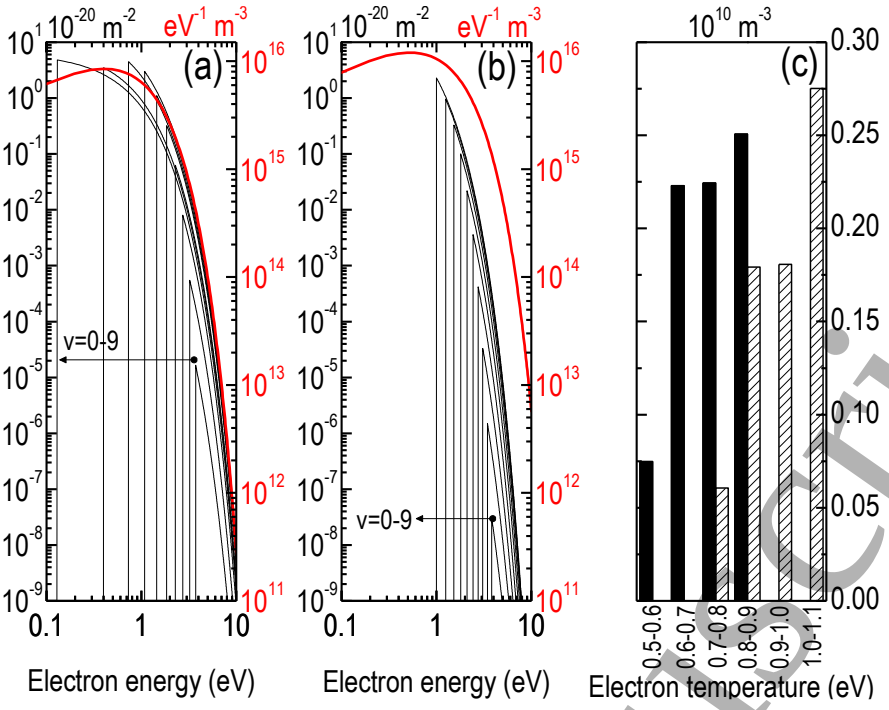

Figure 13. Cross sections of the reactions **(a)** R1/Table III (H_2 case) and **(b)** R2/Table III (D_2 case). *These curves are plotted according to the equation given in Ref. [62] and the available data in Table I of Ref. [61], following the APS permission under the license number RNP/23/MAR/064140.* The red curves correspond to indicative EEDFs of the cold electron population (**Figs. A1** and **A2**; Appendix). **(c)** Histograms of the average values of the negative ion densities over 0.1 eV temperature intervals of the cold electron population; H_2 (solid bars) and D_2 (patterned bars); 1.07 Pa.

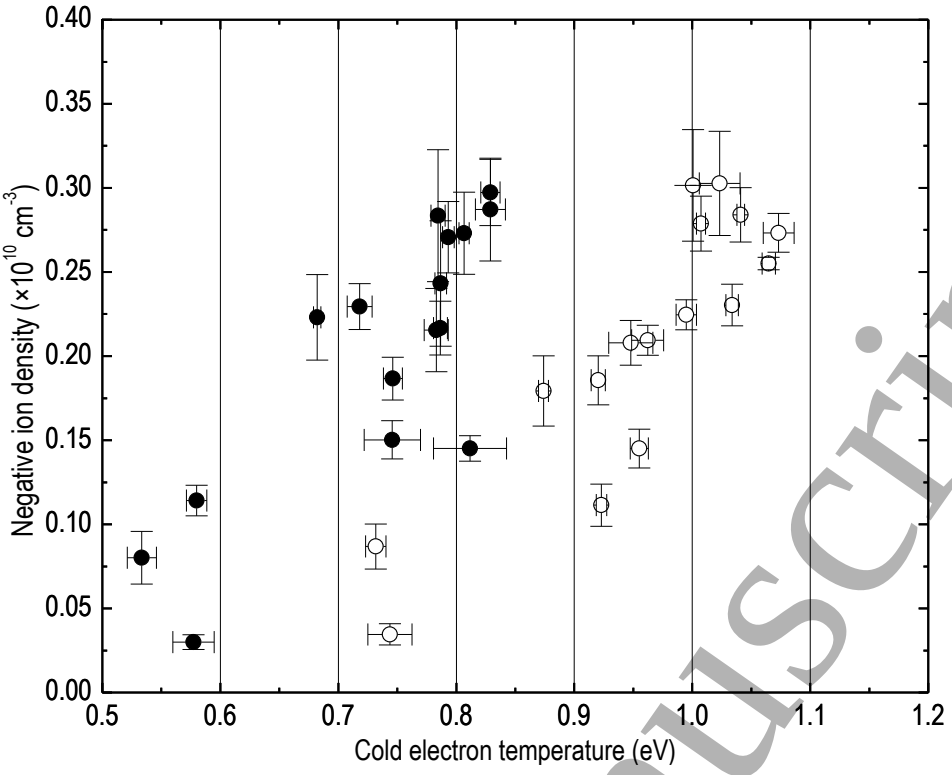

Figure 14. Negative ion density as a function of the cold electron temperature; the data of Figs. 6(b) and 8(b) are combined, by eliminating the power. The grid lines define the temperature intervals where the negative ion density is averaged for getting the histograms of Fig. 13(c). Solid circles: H_2 plasma. Open circles: D_2 plasma.

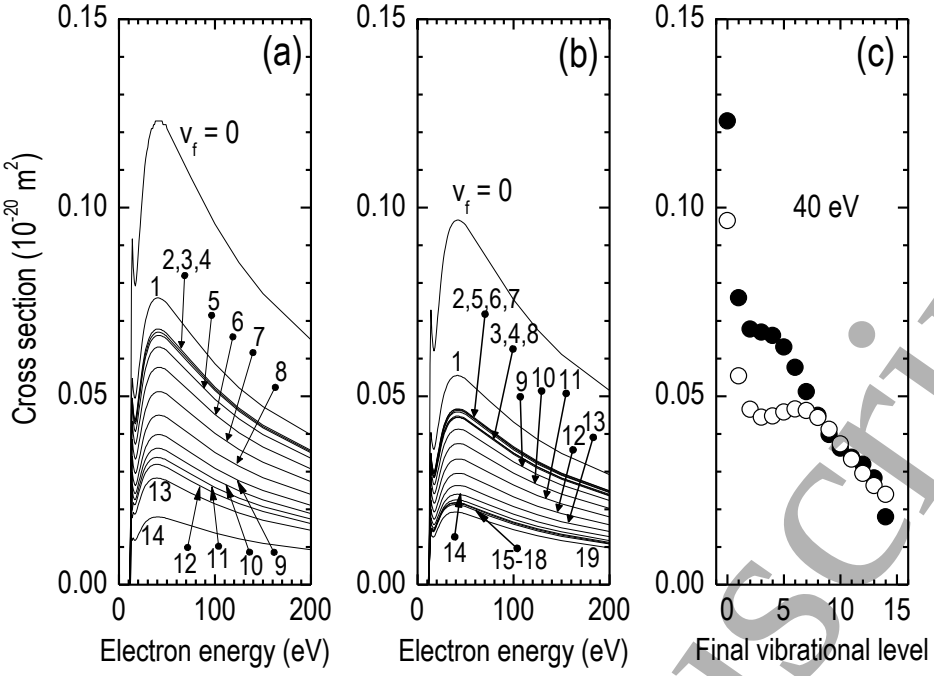

Figure 15. Cross sections of the reaction numbered as **(a)** R41. (H_2) and **(b)** R42. (D_2), in Table IV. The initial vibrational level is $v_i = 0$. *These curves are plotted according to the available data in the online Tables XIX(a1) and XIX(b1) of Ref. [62], following the permission of Prof. Dr. R. Celiberto et al.* **(c)** Comparison of the cross-section values of H_2 (solid circles) and D_2 (open circles) for increasing vibrational level, at an electron energy around 40 eV where the curves peak. Data are collected from Ref. [62].

Table I. Tabulated characteristics of the ECR sources quoted in the text. (Ext.: Extraction aperture; NI: No Information; NA: Not Applicable).

ECR Source	Dimensions	ECR Coupling	Power (kW)	Pressure (Pa)	Gas	Ext.	Te (eV)	$n_{e(cold)}$ (m^{-3})	n_{H^-} (m^{-3})	Extr. Current (mA)
ECR source with driven plasma rings	Aluminum; Ø130 mm × 80 mm	External magnetic discs; 2.45 GHz	max. 0.25 (experiments throughout the range)	0.02 – 0.07	H_2 / D_2	✓	50 – 60	5×10^{16} (0.026 Pa; H_2 [36]).	NI	≤ 4.7 (H_2) ≤ 3.1 (D_2) (0.2 kW)
HOMER	Stainless steel; Ø150 mm × 310 mm (prolonged to 410 mm in [38])	Helmholtz coils; 2.45 GHz	max. 1 (For experiments: 0.2–0.5 [37])	0.3 – 3	H_2 / D_2	✕	0.6 – 1; NI	10^{16} – 10^{17}	≤ 3.9×10^{15} (H_2) [37] Above MoLa (0.3 kW, 0.3 Pa) [39]: ≤ 1.4×10^{15} (H_2), ≤ 1.45×10^{15} (D_2)	NA
Camembert III	Stainless steel; Ø440 mm × 450 mm	7 ECR modules & multicusp field configuration; 2.45 GHz	max. 1.2 (for experiments: 0.5 & 1 [42], 0.9 [44], 1.05 [43])	0.13 –1.07 [42-44]	H_2	✓	Within 0.2 –1.3	In the range of 10^{14} – 10^{16}	≤ 2.6×10^{15}	≤ 0.25 (0.9 kW [44] and 1 kW [42], 0.27 Pa)
ROSAE III	Pyrex cylinder of Ø152 mm × 214 mm housed in a stainless steel cylinder	4 ECR modules; 2.45 GHz	max. 1.2 (For experiments: 0.76 or 0.2 [46] & 1 [47])	0.33 or 1.3 [46]	H_2	✕	0.9; 11 or 2; 6	0.13×10^{16} or 1.4×10^{16}	0.06×10^{15} or 1.7×10^{15}	NA
				0.67 [47]			1.81; 9.45	~ 6.5×10^{15} (Pyrex)	~ 1.5×10^{14} (Pyrex)	
	Quartz cylinder Ø152 mm housed in a stainless steel cylinder [48]	Modified: 1 ECR module; 2.45 GHz	max. 0.2 (for experiments: 0.075 – 0.175)	0.8 or 1.6			0.9 –1.2; NI	~ 4.5×10^{15}	With quartz coverage: ≤ 3×10^{13} or ≤ 5×10^{13}	
SCHEME	Stainless steel; outer dim.: Ø160 mm; inner dim. Ø124 mm × 220 mm (quartz tube) [50]	1 ECR module; 2.45 GHz	max. 0.45 (for experiments: 0.15) [50]	0.8 [50]	H_2 / D_2	✕	~ 1.5; ~ 15	~ 10^{15}	~ 10^{13} (quartz coverage – D_2)	NA
PROMETHEUS I	**Stainless steel; 240 × 240 × 240 mm^{-3}**	**5 ECR modules; 2.45 GHz**	**max. 0.9 (experiments throughout the range)**	**0.13 –2.67**	H_2 / D_2	✕	**0.5 – 2; 12.5 – 17**	**≤ 4.5×10^{16} (H_2); ≤ 7×10^{16} (D_2).**	**≤ 6×10^{15}**	**NA**

Table II. Tabulated information of representative experimental conditions (H_2 / D_2).

Pressure (Pa / mTorr)	**0.15 kW**		**0.9 kW**	
	Flow rate (sccm) (H_2 / D_2)	Wall Temp. (°C) (H_2 / D_2)	Flow rate (sccm) (H_2 / D_2)	Wall Temp. (°C) (H_2 / D_2)
0.53 / 4	6.9 / 8.6	42 / 44	7.4 / 9.2	116.5 / 128.2
1.07 / 8	11.8 / 15.0	41.7 / 43	12.5 / 15.3	119.3 / 120.6
1.60 / 12	16 / 20.1	40.8 / 41.7	16.8 / 20.7	117.4 / 122.2

Table III. Reaction set for the production and destruction of negative ions (* RX denotes: by analogy with the X reaction).

	PRODUCTION		
R1.	$e + H_2(X^1\Sigma_g^+;v) \rightarrow H_2^- \rightarrow H + H^-$	Dissociative Electron Attachment: DEA	[61, 62]
R2.	$e + D_2(X^1\Sigma_g^+;v) \rightarrow D_2^- \rightarrow D + D^-$		
R3.	$e + H_2^+ \rightarrow H^+ + H^-$	Dissociative Recombination: DR	[63, 64]
R4.	$e + D_2^+ \rightarrow D^+ + D^-$		[63, 65]
R5.	$e + H_3^+ \rightarrow H_2^+ + H^-$	Dissociative Recombination: DR	[63]
R6.	$e + D_3^+ \rightarrow D_2^+ + D^-$		
R7.	$e + H_2(v,J) \rightarrow H^- + H^+ + e$	Polar Dissociation	[63]
R8.	$e + D_2(v,J) \rightarrow D^- + D^+ + e$		
R9.	$H_2 + H_2^+ \rightarrow H^- + H + 2H^+$	Ion-Molecule Collisions	[*R11]
R10.	$H_2 + H_2^+ \rightarrow H^- + H^+ + H_2^+$		[*R12]
R11.	$D_2 + D_2^+ \rightarrow D^- + D + 2D^+$		[63]
R12.	$D_2 + D_2^+ \rightarrow D^- + D^+ + D_2^+$		[63]
	DESTRUCTION		
R13.	$H^- + H \rightarrow H_2 + e$	Associative Detachment: AD	[66]
R14.	$D^- + D \rightarrow D_2 + e$		
R15.	$H^- + H \rightarrow H_2(v) + e$	Associative Detachment (AD) with creation of vibrationally excited molecules	[67]
R16.	$D^- + D \rightarrow D_2(v) + e$		[*R15]
R17.	$H^- + H \rightarrow 2H + e$	non-Associative Detachment: non-AD	[68]
R18.	$D^- + D \rightarrow 2D + e$		[63]
R19.	$H^- + e \rightarrow H + 2e$	Electron Detachment: ED	[68]
R20.	$D^- + e \rightarrow D + 2e$		[63]
R21.	$H^- + H_2(v) \rightarrow H_2(v\text{-}2) + H + e,\ 2 \le v \le 6$	Electron Detachment in collisions with vibrationally excited molecules: EDV	[69, 70]
R22.	$D^- + D_2(v) \rightarrow D_2(v\text{-}2) + D + e,\ 2 \le v \le 6$		[*R21]
R23.	$H^- + H_2 \rightarrow H_2 + H + e$	Collisional Detachment: CD	[71]
R24.	$D^- + D_2 \rightarrow D_2 + D + e$		
R25.	$H^- + H^+ \rightarrow 2H$	Mutual Neutralization: MN	[69, 72]
R26.	$H^- + H^+ \rightarrow H + H(n=2, 3)$		[69, 73]
R27.	$H^- + H_2^+ \rightarrow H_2 + H$		[69, 73]
R28.	$H^- + H_2^+ \rightarrow 3H$		[69, 72]
R29.	$H^- + H_2^+ \rightarrow H + H_2(v)$		[67]
R30.	$H^- + H_3^+ \rightarrow 2H_2$		[69, 73]
R31.	$H^- + H_3^+ \rightarrow 4H$		[69, 72]
R32.	$H^- + H_3^+ \rightarrow 2H + H_2(v)$		[67]
R33.	$D^- + D^+ \rightarrow 2D$		[*R25]
R34.	$D^- + D^+ \rightarrow D + D(n=2, 3)$		[*R26]
R35.	$D^- + D_2^+ \rightarrow D_2 + D$		[*R27]
			[*R28]

R36.	$D^- + D_2^+ \rightarrow 3D$	[*R29]
R37.	$D^- + D_2^+ \rightarrow D + D_2(v)$	[*R30]
R38.	$D^- + D_3^+ \rightarrow 2D_2$	[*R31]
R39.	$D^- + D_3^+ \rightarrow 4D$	[*R32]
R40.	$D^- + D_3^+ \rightarrow 2D + D_2(v)$	

Table IV. Representative reactions for the population and de-excitation of vibrational states (* RX denotes: by analogy with the X reaction).

EXCITATION			
R41.	$H_2(X^1\Sigma_g^+; v_i) + e \rightarrow H_2(X^1\Sigma_g^+; v_f) + e$, $v_f > v_i$	Resonant electron-vibration excitation: eV	[74]
R42.	$D_2(X^1\Sigma_g^+; v_i) + e \rightarrow D_2(X^1\Sigma_g^+; v_f) + e$, $v_f > v_i$		
R43.	$H_2(X^1\Sigma_g^+; v_i) + e \rightarrow H_2(B^1\Sigma_u^+, C^1\Pi_u) + e \rightarrow H_2(X^1\Sigma_g^+; v_f) + e + hv$, $v_f > v_i$	Radiative decay and excitation: EV	[62]
R44.	$D_2(X^1\Sigma_g^+; v_i) + e \rightarrow D_2(B^1\Sigma_u^+, C^1\Pi_u) + e \rightarrow D_2(X^1\Sigma_g^+; v_f) + e + hv$, $v_f > v_i$		
R45.	$H(wall) + H(wall) \rightarrow H_2(v)$	Recombinative Desorption: Langmuir–Hinshelwood	[75]
R46.	$D(wall) + D(wall) \rightarrow D_2(v)$		
R47.	$H(gas) + H(wall) \rightarrow H_2(v)$	Eley–Rideal	[76]
R48.	$D(gas) + D(wall) \rightarrow D_2(v)$		
R49.	$H(wall^*) + H(wall) \rightarrow H_2(v)$	*Where, H/D(wall*), refers to a "weakly bound" atom on the surface*	'Hot–atom' (Harris–Kasemo)	[77]
R50.	$D(wall^*) + D(wall) \rightarrow D_2(v)$		
DE-EXCITATION			
R51.	$H_2(v_i) + H \rightarrow H_2(v_f) + H$, $v_f < v_i$	Vibrational-translational relaxation in collisions with atoms: V-t	[69, 78] [13]
R52.	$D_2(v_i) + D \rightarrow D_2(v_f) + D$, $v_f < v_i$		
R53.	$H_2(v_i) + H_2(v_j) \rightarrow H_2(v_i) + H_2(v_j\text{-}1)$	Vibrational-translational relaxation in collisions with molecules: V-T	[73] [13]
R54.	$D_2(v_i) + D_2(v_j) \rightarrow D_2(v_i) + D_2(v_j\text{-}1)$		
R55.	$H_2(v_i) + wall \rightarrow H_2(v_f)$, $v_f < v_i$	Wall relaxation: WD	[69, 79] [13]
R56.	$D_2(v_i) + wall \rightarrow D_2(v_f)$, $v_f < v_i$		

Appendix

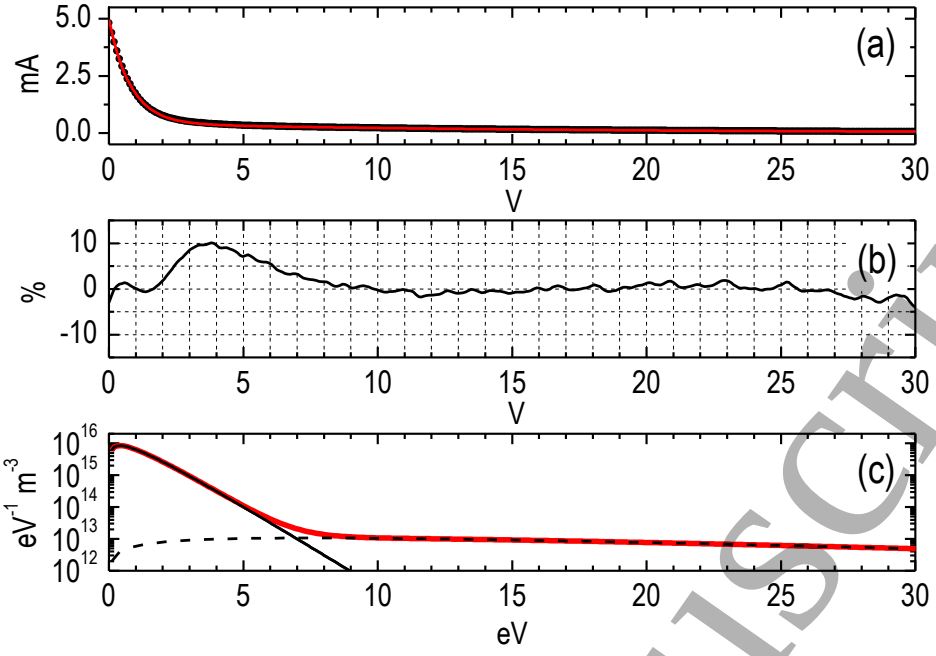

Figure A1. Representative example from the H_2 plasma (1.07 Pa, 0.75 kW). **(a)** Bi-Maxwellian fitting (red line) to the experimentally determined electron current (black solid circles), versus the absolute value of the difference between the probe bias and the plasma potential. **(b)** Percentage of the residuals of the fiiting process. **(c)** EEDF (red line) based on the bi-Maxwellian assumption; cold population part (black solid line; 0.81 eV); hot population part (black dashed line; 15.32 eV).

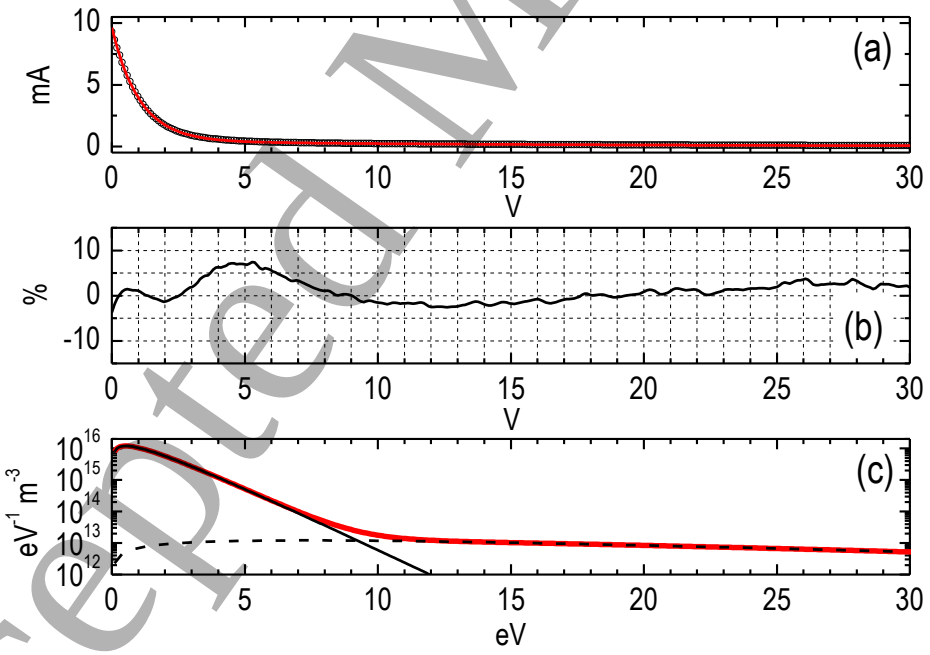

Figure A2. Representative example from the D_2 plasma (1.07 Pa, 0.75 kW). **(a)** Bi-Maxwellian fitting (red line) to the experimentally determined electron current (black open circles), versus the absolute value of the difference between the probe bias and the plasma potential. **(b)** Percentage of the residuals of the fiiting process. **(c)** EEDF (red line) based on the bi-Maxwellian assumption; cold population part (black solid line; 1.04 eV); hot population part (black dashed line; 14.65 eV).

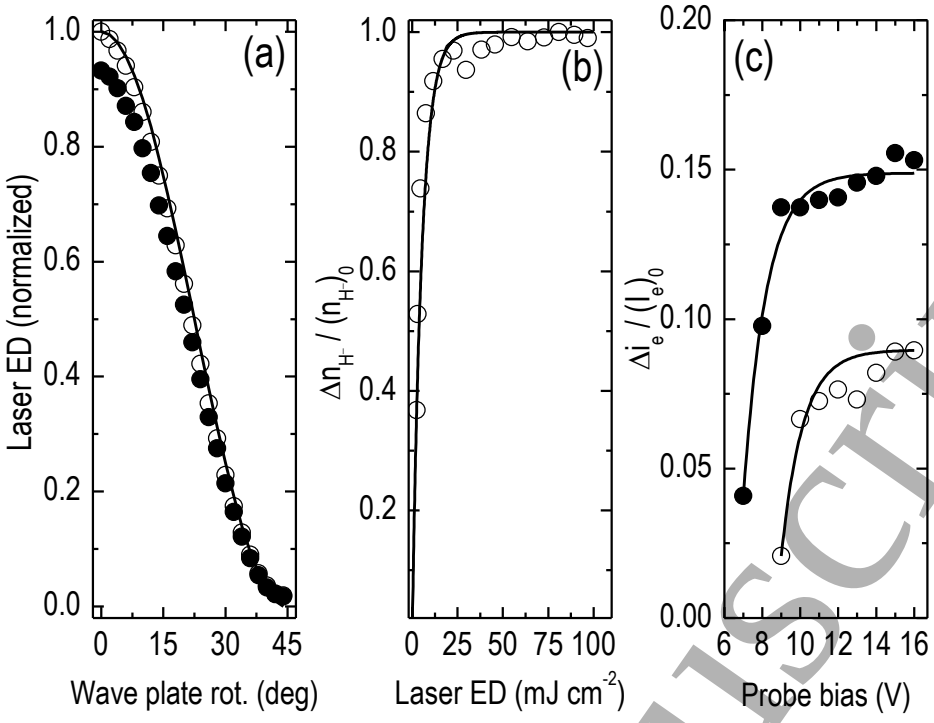

Figure A3. (a) Normalized attenuation curves of the laser beam energy density (ED). Line: Malus' law; Open circles: measurements in front of a viewport; Solid circles: measurements behind a single glass viewport. **(b)** Ratio of the photo-destructed negative ion density Δn_{H^-} to the saturation density $(n_{H^-})_0$, as a function of the laser beam ED. Line: theory [56]; Open circles: experiments at 2.0 Pa of H_2 and 0.9 kW. **(c)** Ratio of the photodetachment signal peak (due to the instantaneously photodetached electrons) (Δi_e) to the steady state electron current $(I_e)_0$, as a function of the probe bias voltage. Open circles: 1.60 Pa of D_2 and 0.9 kW; Solid circles: 1.60 Pa of H_2 and 0.9 kW. Lines: exponential fitting.

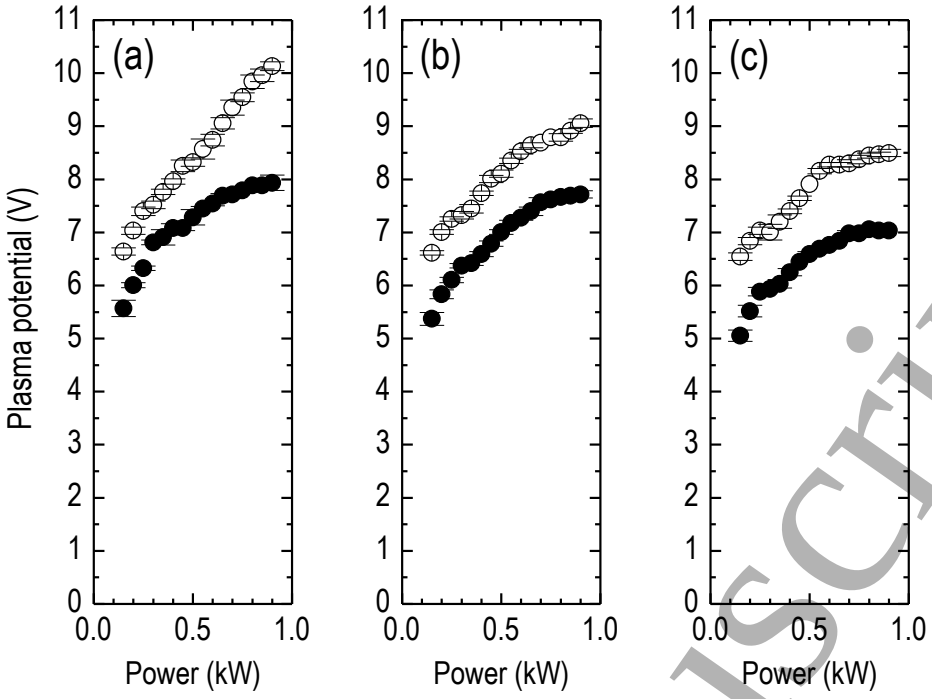

Figure A4. Plasma potential as a function of the MW power at **(a)** 0.53 Pa, **(b)** 1.07 Pa, and **(c)** 1.60 Pa. Solid circles: H_2 plasma. Open circles: D_2 plasma. Mean values and standard deviations are derived from four series of experiments (2 sets at 2 different dates).